Effects of Tip Clearance and Surface Roughness on Small-Scale Turbopump Impeller Performance

by

Kinjal A. L. Ruecker

Submitted to the Department of Aeronautics and Astronautics
in partial fulfillment of the requirements for the degree of

MASTERS OF SCIENCE IN AEROSPACE ENGINEERING

at the

MASSACHUSETTS INSTITUTE OF TECHNOLOGY

September 2024

Authored by: Kinjal A. L. Ruecker
Department of Aeronautics and Astronautics
July 8, 2024

Certified by: Zoltán S. Spakovszky
T. Wilson (1953) Professor in Aeronautics, Thesis Supervisor
Head, Air Sector
Director, Gas Turbine Laboratory

Certified by: Zachary Cordero
Associate Professor of Aeronautics and Astronautics,
Thesis Supervisor

Accepted by: Jonathan P. How
Department of Aeronautics and Astronautics
Richard C. Maclaurin Professor of Aeronautics and Astronautics

Effects of Tip Clearance and Surface Roughness on Small-Scale Turbopump Impeller Performance

by

Kinjal A. L. Ruecker

Submitted to the Department of Aeronautics and Astronautics
on July 8, 2024 in partial fulfillment of the requirements for the degree of

MASTERS OF SCIENCE IN AEROSPACE ENGINEERING

ABSTRACT

Centimeter-scale turbopump impellers typically used in liquid rocket engines of small launch vehicles suffer from reduced performance due to manufacturing challenges and non-uniform geometric scaling.

This thesis aims to characterize the impact of impeller blade tip clearance and surface roughness on the performance of small-scale turbopump impellers by assessing the dominant flow features, quantifying the underlying loss mechanisms, and determining the sensitivity of performance losses to changes in tip clearance and surface roughness. The study identifies the primary flow features governing impeller performance to be blade tip leakage flow and secondary flow.

The analysis identified two distinct flow regimes based on tip clearance: above 5% of tip clearance, the losses are predominantly due to blade tip leakage flow, whereas below this threshold, losses are governed by both secondary flow and blade tip leakage flow. For tip clearances above 5% of the blade span, blade tip leakage flow is estimated to contribute more than 80% of total impeller loss. A 1% change in tip clearance is estimated to result in a 0.8% loss in efficiency. The calculations suggest increasing surface roughness reduces the effective tip clearance due to increased viscous effects in the tip gap, but strengthens the secondary flow. This lowers the effective tip clearance that separates the flow regimes. The contribution of blade tip leakage loss to total impeller loss decreases by up to 22% for surface roughness increased from an R_a value of 1 μm to 10 μm. The strengthened secondary flow at higher surface roughness increases mixing of the blade tip leakage flow with the blade passage flow, leading to larger regions of blockage. Increasing the surface roughness from an R_a value of 1 μm to 10 μm results in a 4% loss in impeller efficiency.

This study demonstrates that surface roughness is more impactful on small-scale impeller performance than blade tip clearance, and so manufacturing for smooth surfaces should be prioritized over reducing the blade tip clearance gap.

Thesis supervisor: Zoltán S. Spakovszky
Title: T. Wilson (1953) Professor in Aeronautics

Acknowledgments

To my advisors, Dr. Spakovszky and Dr. Cordero, for their insightful feedback in shaping this work and my academic journey as a whole.

To the lab research engineer, David Cuadrado, for weekend computational support.

To my decrepit desk-mate, Vaishnavi, for sharing her hard-earned wisdom in research life.

To my benchwarmers, Shaan, Lanie, Alisa, Kaila and Maranda, for riding the roller coaster that is MIT with me the past two years.

To my chosen family, Melissa, Anielle, Gwyn and Valeria, for their unconditional love and belly laughs whenever we talk.

To my parents, Bhavya and Lukas, for a lifetime of encouragement and sacrifices for me to be where and who I am.

And to the most important person in my life. The person who makes me kinder. The calm to my fire. My husband, Hunter.

Contents

List of Figures

List of Tables

Chapter 1

Introduction

1.1 Background and Motivation

In liquid fueled rockets, turbopump impellers pressurize propellants to high levels required by the engine's thrust chamber. A schematic cross-section of a typical rocket engine turbopump is illustrated in Figure 1.1. Unlike impellers used in industrial applications such as power stations, marine propulsion, boilers, sewage, or irrigation systems, rocket engine impellers operate under challenging conditions: they achieve tip speeds up to 500 m/s, handle flow rates up to 1.6 m^3/s for both corrosive and cryogenic fluids, and manage head rises up to 15,000 m, all while accommodating rapid start and shutdown transients [1][2].

Rocket engine turbopump impellers with centimeter-scale diameters are used in propulsion systems of large satellites and probes, small lunar-landers, upper stage vehicles, and other mission architectures that benefit from having less parasitic mass compared to pressure-fed engines. Small-scale impellers[1] are enabled by their ability to be vertically integrated within companies, allowing industry to develop bespoke turbomachinery for a specific performance target. This is in part due to lower cost and less infrastructure required for build and assembly, but also by additive manufacturing (AM) techniques and novel printable

[1] In this thesis, small-scale refers to impellers with centimeter scale diameters

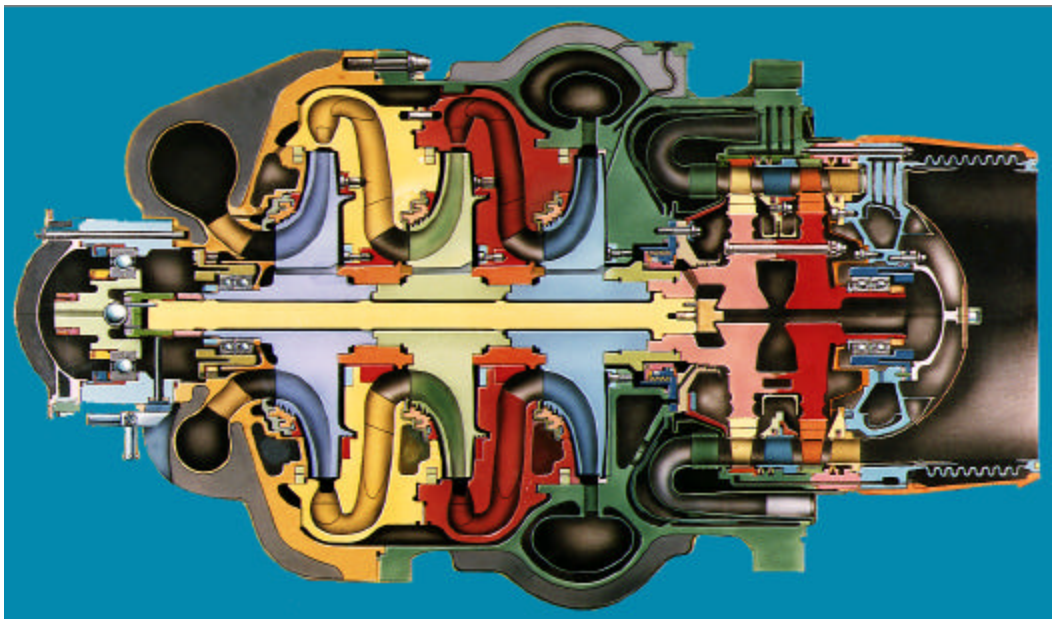

Figure 1.1: The high-pressure fuel turbopump for the RS-25 engine [3] used for NASA's Space Shuttle missions and Space Launch System. A stage consists of an impeller (purple) and a diffuser(yellow).

materials. AM enables the end-to-end development of centimeter-scale impellers through quick prototyping, small production runs [4], and enhanced part resilience by customizing microstructures in the light of adverse operational environments of rocket engines [5]. The limitation of print size imposed by AM makes it particularly well-suited for the fabrication of small components.

The design of impellers is often streamlined by scaling existing geometries to meet new specifications. However, this approach presents two challenges for small-scale impeller design: maintaining fluid dynamic and geometric similarity relative to larger impellers, and dealing with the increased relative roughness resulting from the manufacturing process. Table 1.1 compares the impeller design point for the RS-25 engine used on the Space Shuttle and Space Launch System [3] and the small-scale impeller investigated here. The Reynolds number for this comparison is defined based on tip speed. Since both impellers operate in the fully turbulent regime, it then follows that flow features and loss mechanisms remain consistent for scaled impellers maintaining geometric and aerodynamic similarity [1]. This similarity

is not maintained in small-scale impellers because the relative change in geometry during operation and in surface roughness (roughness does not scale) are higher compared to large impellers. Variations in performance that arise from these two effects form the basis for characterizing the performance of small-scale impellers, and are the focus of this research.

Property	Unit	Small-Scale Impeller	RS-25
Fluid	–	lCH_4	lH_2
Kin. Viscosity	$\mu\ m^2/s$	0.2411	0.1736
Radius	m	0.022	0.1325
Design Speed	rpm	140000	34360
Tip Speed	m/s	323	477
Reynolds Number	–	2.21e7	2.58e8

Table 1.1: Comparison between the small-scale and large impellers. The radius for the RS-25 impeller is estimated from visuals provided by Rocketdyne [3].

1.2 Problem Statement and Research Objectives

This research aims to investigate how impeller blade tip clearance and surface roughness affect the performance and efficiency of small-scale turbopump impellers under the assumption that fluid dynamic and geometric similitude to larger impellers cannot be maintained in operation or manufacturing. A focus is placed on characterizing the key flow features and loss mechanisms across varying blade tip clearances and surface roughness.

The following research questions are addressed:

- What are the dominating flow features that drive loss in a small-scale impeller? What are the loss mechanisms associated with these flow features?
- Does the dominating loss mechanism change at different clearances and roughness? If so, how and why?
- How do the effects of tip clearance and surface roughness on small-scale impellers compare relative to a large-scale impeller?

This thesis demonstrates that the dominant flow features in a small-scale impeller are blade tip leakage flow and secondary flow. The flow field can be categorized into two distinct regimes based on the dominant loss mechanism: blade tip leakage flow prevails at higher clearances, while secondary flow becomes the primary source of loss at lower clearances.

The work also shows that surface roughness has a greater impact on loss than blade tip leakage flow when using AM methods. At a surface roughness R_a of 10 μm, the contribution of blade tip leakage flow to total impeller loss is between 15% for 2.5% tip clearance, and 56% for 10% tip clearance.

The computations suggest that for small-scale impellers a 1% change in tip clearance results in a 0.8% loss in efficiency, and that increasing the surface roughness R_a from a value of 1 to 10 μm yields a 4% loss in impeller isentropic efficiency.

1.3 Approach

The hypothesis is that blade tip leakage flow is the dominant flow feature governing small-scale impeller performance. Though the flow characteristics and loss mechanisms exhibited by turbopump impellers are highly three dimensional, Gülich [1] highlights the importance of employing one-dimensional modeling for estimating performance. This approach views the effects of blade tip clearance and surface roughness from an overall impeller performance standpoint, and aligns with Denton's recommendation to analyze the sensitivity of total entropy production to tip clearance area to estimate mixing loss [6]. The simplified model of the blade tip leakage jet presented by Storer and Cumpsty [7], is used to estimate the contributions of blade tip leakage loss to overall impeller loss. Parameter sweeps over mass flow ratio, pressure ratio, jet injection angle, and clearance size are carried out to identify the key drivers for loss.

It is expected that higher relative roughness will lead to increased loss. The mechanism behind this is viscous dissipation in the boundary layers. Given that the small-scale impeller

operates at a high Reynolds number of 12 million and exhibits higher relative roughness due to its small geometry, it is anticipated that the flow will be hydraulically rough. Consequently, performance is expected to remain unchanged with further increases in Reynolds number beyond the threshold for hydraulically rough flow [8]. Sensitivity to surface roughness will thus focus only on the R_a value.

Two computational studies are conducted to explore the effects of tip clearance and of surface roughness on impeller performance in isolation. The tip clearance percentage is defined as the ratio of clearance height over the exit blade span. The test matrix is outlined in Table 1.2 with the baseline case being 5% blade tip clearance with a smooth surface. The selected tip clearances are consistent with common values in typical rocket engine turbopumps [9]. Figure 1.2 illustrates the small-scale impeller under study[2].

TC \ R_a	smooth	1 μm	10 μm
2.5%	•	•	•
5.0%	Baseline	•	•
10%	•	•	•

Table 1.2: Test matrix to assess effects of blade tip clearance and surface roughness on impeller performance.

[2]Courtesy of David Gregory of New Frontier Aerospace.

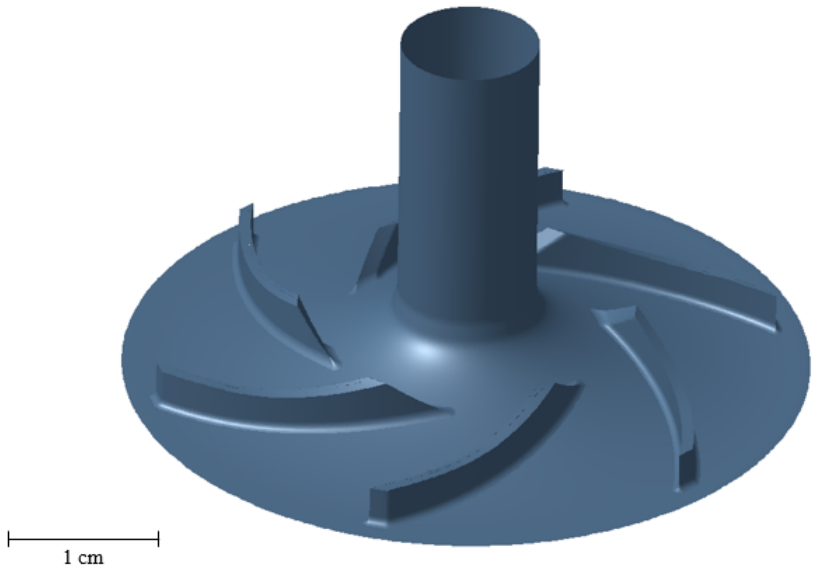

Figure 1.2: Centimeter-scale impeller geometry used in parametric study.

Chapter 2

Overview of Relevant Concepts

This chapter first introduces concepts relevant to impeller blade tip clearance and surface roughness. Literature is presented for comparable experimental results, and due to the scarcity of data specific to rocket applications, insights from radial compressors are presented as well. A 1% increase in blade tip clearance lowers efficiency by 1% for rocket turbopumps and 0.6% for centrifugal compressors. Roughness effects consistently decrease efficiency across different machine types. For similar roughness to the small-scale impeller under study, efficiency is expected to reduce between 2% and 9%. These findings substantiate the computational results of this research in the absence of experimental data on the specific small-scale impeller analyzed.

The chapter then demonstrates Reynolds number independence across blade tip clearances and surfaces with an R_a of 1 μm and 10 μm, noting that the small-scale impeller operates in the fully turbulent regime for both pipe and flat plate Reynolds numbers. This allows evaluation of variable blade tip clearance and surface roughness effects at a single Reynolds number, reducing the dimensionality required for the parametric study.

2.1 Effect of Tip Clearance on Efficiency

The clearances between stationary and rotating components, sketched in Figure 2.1, are the radial clearance between the impeller hub and volute, and the axial blade tip clearance between the impeller blade and shroud. The focus here is on axial blade tip clearance, as radial clearance are influenced by adjacent components and design features such as balancing holes [10], and does not affect the flow in the blade passage.

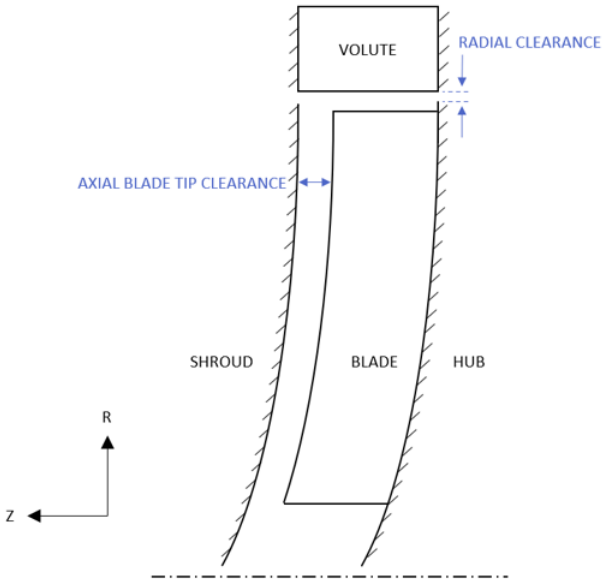

Figure 2.1: Definition of axial blade tip clearance in an unshrouded impeller.

A typical blade tip clearance for a launch vehicle impeller is approximately 3.5% of the exit blade span [9]. Additionally, blade tip clearances can change during operation, induced by centripetal growth, thermal expansion/contraction, housing deflection, and thrust balancing [11]. Besides changes in operation, blade tip clearance is affected by inconsistencies in production and assembly, such as an unfavorable tolerance stack-up. A change in blade tip clearance can cause a distinct shift in the characteristic as illustrated in Figure 2.2. For a set flow rate (x-value), increased blade tip clearance reduces the resultant head rise (y-value).

Studies on the impact of blade tip clearance on impeller efficiency for unshrouded, centrifugal machines (Table 2.1) revealed an average 0.9% performance degradation with a 1%

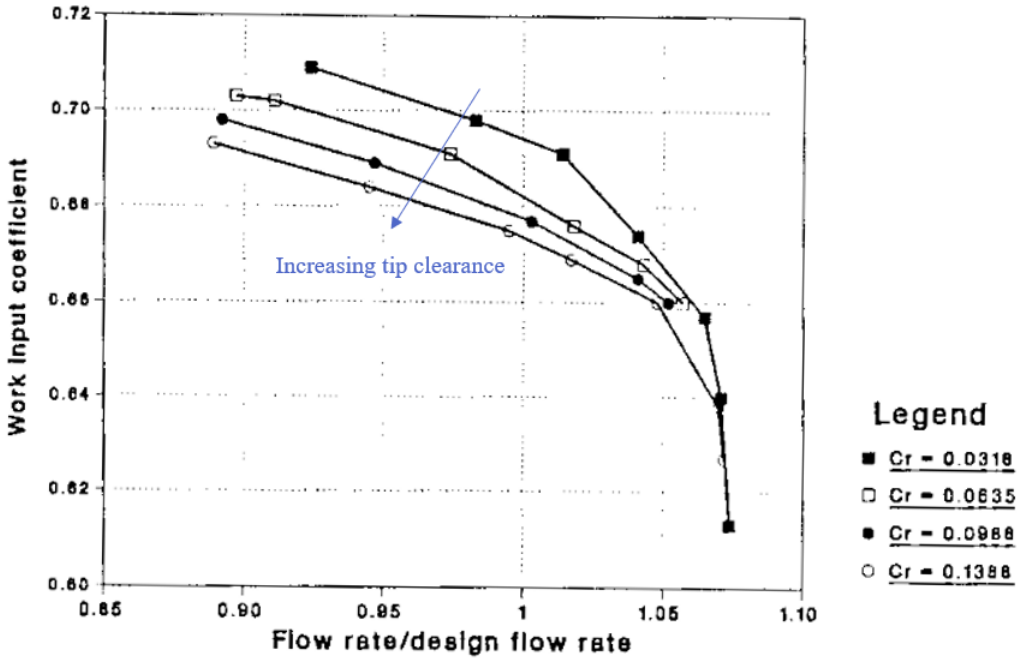

Figure 2.2: Impact of blade tip clearance on the impeller characteristic. [12].

increase in tip clearance for turbopump impellers, and an average 0.5% loss for compressor impellers.

Benefits of unshrouded impellers include lower cost and parasitic mass. Hoshide and Nielson [9] and Chen et al. [11] investigated the impacts on cost and performance of an unshrouded J-2 turbopump. Water tests demonstrated a 12% decrease in efficiency with a 10% increase in blade tip clearance. Similarly, another study by Williams et al. [13]-[14] explored how an unshrouded impeller increases the payload capacity of a launch vehicle. Their tests for the unshrouded Space Shuttle Main Engine High Pressure Fuel Turbopump (SSME HPFTP) with liquid hydrogen observed a 12% decrease in efficiency when the blade tip clearance was increased by 15%.

Outside of rocket-specific applications, Engeda et al. [15] looked at blade tip clearance effects in centrifugal impellers for pumps. They revealed that higher specific speeds resulted in increased sensitivity to changes in blade tip clearance. At a specific speed similar to that of the small impeller under investigation in this study, there was an efficiency loss of 6%

with an increase in blade tip clearance from 2.5% to 10%.

An investigation of compressor impellers also provided insight into blade tip clearance sensitivity. Senoo and Ishida [16] report a 4% drop in efficiency with a blade tip clearance increase from 0 (shrouded) to 10% for a compilation of published compressor data. Additionally, they found that low-pressure-ratio compressors are more susceptible to efficiency losses from blade tip clearance. The study by Ishida et al. [17] that looked at blade tip geometries found for a sharp edge, similar to the blade in the small-scale impeller within this study, the efficiency loss was 6% for a 10% increase in blade tip clearance. Experiments by Brasz [12] saw a loss of 4% efficiency for an increase in tip clearance of 10% for a centrifugal compressor operating at design (max efficiency). Brasz additionally shared data from ten other blade tip clearance centrifugal compressor studies, their results ranging between a 0.08% and 0.62% decrease in efficiency.

From the results in Table 2.1, it is evident that turbopump impellers are more sensitive to tip clearance than compressor impellers. Results from this thesis are expected to be closer to the decrease in efficiency seen by turbopumps, the same machine as the small-scale impeller under study. Additionally, little research has been published on tip clearance for centimeter-scale impellers. The impellers in the literature summarized in Table 2.1 are 3 to 12x larger than the impeller in this study.

Reference	Centrifugal Machine	⌀ [m]	ϕ	ψ	$\Delta\eta/\Delta$TC
Hoshide & Nielson [9] Chen et al. [11]	Rocket impeller	0.30	0.11	0.63	1.2%
Williams et al. [13], [14]	Rocket impeller	0.20	0.12	0.53	0.8%
Engeda et al. [15]	Pump impeller	0.27	0.2	-	0.8%
Senoo & Ishida [16]	Compressor impeller	0.15	-	0.75	0.4%
Ishida et al. [17]	Compressor impeller	0.51	0.27	0.6	0.6%
Brasz [12]	Compressor	0.52	-	0.7	0.4%

Table 2.1: Pertinent literature for unshrouded impellers shows a higher sensitivity to changes in blade tip clearance for rocket impellers compared to centrifugal compressors. For each reference, operating flow coefficients (ϕ) and pressure coefficients (ψ) were estimated from the provided data.

2.2 Effect of Surface Roughness on Efficiency

Surface roughness is primarily influenced by the manufacturing method and subsequent surface treatment. Average surface roughness, R_a, is defined through an average height of the peaks and valleys relative to the average center line of the surface profile [18]. For common manufacturing methods, the R_a value ranges between 0.2 and 1100 μm, seen in Figure 2.3, with additive manufacturing (AM) modalities resulting in a higher average surface roughness than conventional processes. For small-scale additively manufactured turbopump impellers that have an order of magnitude higher relative roughness compared to larger pumps, surface roughness can strongly impact performance.

Figure 2.3: Surface roughness for AM processes are higher than typical manufacturing processes, adapted from Gradl [18].

In analyzing surface roughness effects, an "equivalent" grain with constant spacing and diameter is used because grains composing a real surface are not uniform in spacing or protrusion into the flow. This equivalent sand grain roughness (k_s) is used to estimate the impact of the real surface on skin friction losses [19]. The relationship between R_a and k_s is

often derived experimentally for a specific surface roughness and material. Open literature shows the relationship can vary by up to a factor of 5 for different turbine blade surface types [19]. This study applies a relationship posited by Adams et al. [20] that used a monolayer of uniform diameter spheres to theoretically derive a relationship between R_a and k_s rather than rely on empirical analysis alone. The generalized algorithm is shown in Equation 2.1, though specific AM pump surfaces should be tested for a better correlation.

$$k_s = 5.863\ R_a \tag{2.1}$$

Surface roughness classified by k_s can be categorized as hydraulically smooth, transitionally rough, or fully rough, as depicted in Figure 2.4. As relative roughness increases, the classification shifts towards fully rough, affecting the turbulent flow structure as the grain peaks protrude through the laminar sublayer. Once past the fully rough transition point, there is no change in performance with Reynolds number [8]. Blades are typically designed to remain within the hydraulically smooth regime, with the permissible k_s defined by Schlichting in Equation 2.2 [19], where ν is kinematic viscosity, and w is relative velocity. The k_s defining the transition to fully rough surfaces is ten times the permissible k_s [1].

$$k_{s,smooth} < \frac{100\nu}{w} < k_{s,transition} < \frac{1000\nu}{w} < k_{s,fully\ rough} \tag{2.2}$$

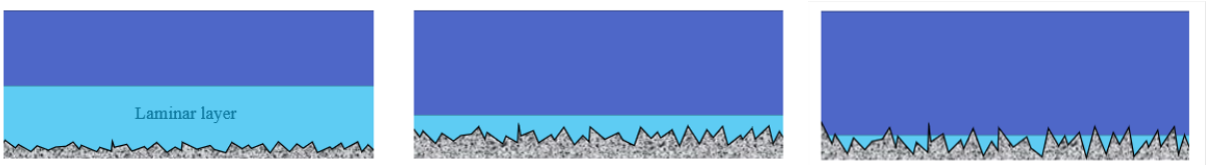

(a) Hydraulically smooth (b) Transitionally rough (c) Fully rough

Figure 2.4: The small-scale impeller operates in the fully rough surface regime.

Due to the compact size, high operating speeds, and utilization of cryogenic fluids, the permissible surface roughness (R_a) associated with k_s as defined in Equation 2.2 is constrained to 0.01 μm for the small-scale impeller in this study. This R_a is unachievable

through the conventional manufacturing techniques listed in Figure 2.3, so consequently, the small-scale impeller is subject to fully rough surfaces. This study aims to evaluate the effect of varying surface roughness values, specifically R_a between 1 and 10 μm (k_s between 6 and 60 μm, respectively) encompassing seven out of the ten commonly employed manufacturing methods illustrated in Figure 2.3.

Existing literature examining similar sand grain roughness factors (k_s) to those of the impeller under investigation, summarized in Table 2.2, suggest a potential efficiency decrease of up to 10% when comparing smooth wall conditions to R_a values in the tens of microns. Gulich [21] conducted a comprehensive analysis incorporating experimental data from 19 pumps, featuring k_s values spanning from 1 to 130 μm, with pertinent findings highlighted in Figure 2.5. Notably, when roughness is uniformly applied to all surfaces within the pump, a reduction in efficiency of up to 10% is observed.

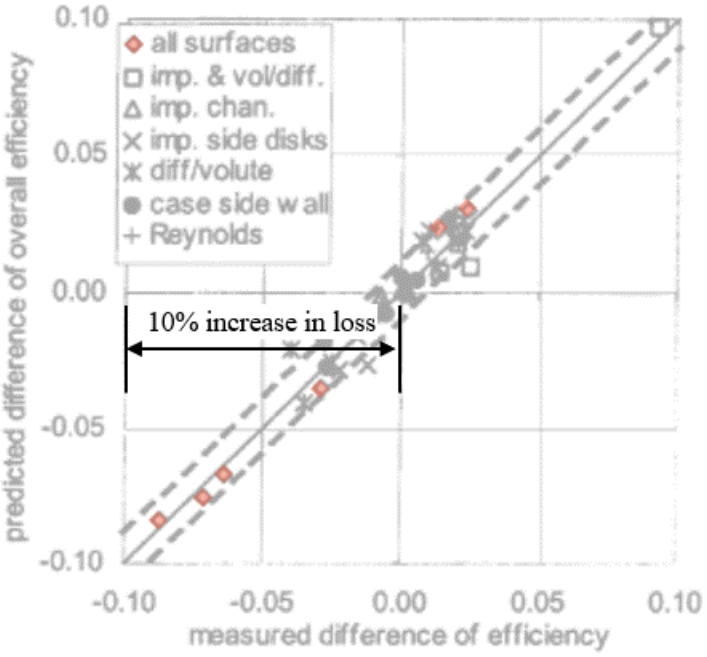

Figure 2.5: Up to 10% decrease in efficiency due to surface roughness for 19 pumps with k_s ranging from 1 to 130 μm [21].

Similarly, computational investigations by He [22] corroborate these empirical findings. Simulations at a k_s of 40 μm indicate that rough surfaces yield an efficiency drop of more

than 9% when compared to smooth surfaces. Figure 2.6 is an adaptation of relevant results from this study, distinguishing between different simulation cases. The simulations for case 1 had no rough parts, while case 7 had all rough parts.

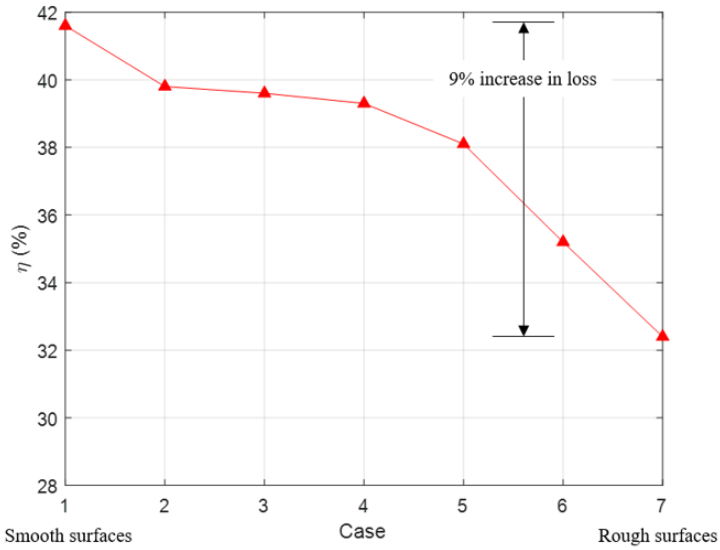

Figure 2.6: When all surfaces are rough (R_a of 40μm), efficiency decreases by 9% [22].

Moreover, in a comprehensive survey paper by Bons [19], research conducted on NACA-65 blade profiles by Bammert and Milsch [23] and Bammert and Woelk [24] estimated losses ranging from 2% to 13%. Although axial compressors differ from centrifugal pumps, the congruent findings across these studies for comparable surface roughness to this study support the anticipated loss due to surface roughness.

Bons [19] also observes a notable trend for radial compressors wherein roughness effects become substantial at a $\frac{k_s}{d_{hydraulic}}$ ratio of approximately $3e^{-4}$, similar to the conditions encountered by the small-scale impeller under study with an R_a of 10 μm.

Reference	Machine	k_s [μm]	$\Delta\eta$
Gulich [21]	Centrifugal pumps	1 to 130	3-10%
He [22]	Centrifugal pump	40	9%
Bammert and Milsch [23]	Axial compressor	41.4 to 1000	2-10%
Bammert and Woelk [24]	Axial compressor	60 to 180	6-13%

Table 2.2: Decrease in efficiency from rough surfaces is consistent across machine type.

2.3 Reynolds Number Independence

Reynolds number is a dimensionless parameter that relates the inertial forces to the viscous forces within a fluid, as defined in Equation 2.3 [25]. It incorporates the characteristic velocity (V), kinematic viscosity (ν), and length scale (L) of the flow.

$$\mathrm{Re} = \frac{VL}{\nu} \tag{2.3}$$

From a one-dimensional perspective, viscous flow through an impeller passage can be approximated by either pipe flow or flat plate flow, depending on the geometry. The Reynolds number for pipe flow and flat plate flow is defined using different characteristic lengths governed by the interaction between the viscous layer and either the core flow (pipe flow) or the free stream (flat plate flow). The characteristic length in the context of pipe flow is the hydraulic diameter, determined by the exit blade span and passage width. For flat plate flow, the characteristic length is the blade chord, which has been shown by Casey and Robinson [8] to better represent internal flows compared to diameter-based Reynolds numbers. The flat plate based Reynolds number is used in this thesis. However, regardless of the definition used, the small-scale impeller operates within the fully turbulent regime (Figure 2.7). In the fully turbulent regime, once the upper critical Reynolds number is exceeded, performance changes become independent of the Reynolds number [8][26].

Variations in tip clearance and surface roughness were investigated to assess Reynolds independence. Figure 2.8 shows Reynolds independence across three different clearances at four operating speeds and three flow rates for smooth wall simulations. Additionally, the variation in surface roughness R_a of 1 μm and 10 μm for 5% tip clearance at a constant flow rate was investigated (Figure 2.9). The head rise for rough surfaces being similar despite a lower efficiency will be further explained in Section 6.1. The analyses show that pressure rise and impeller efficiency remain constant across the range of clearances and operating conditions, meeting the expected trend of Reynolds independence for fully rough surfaces.

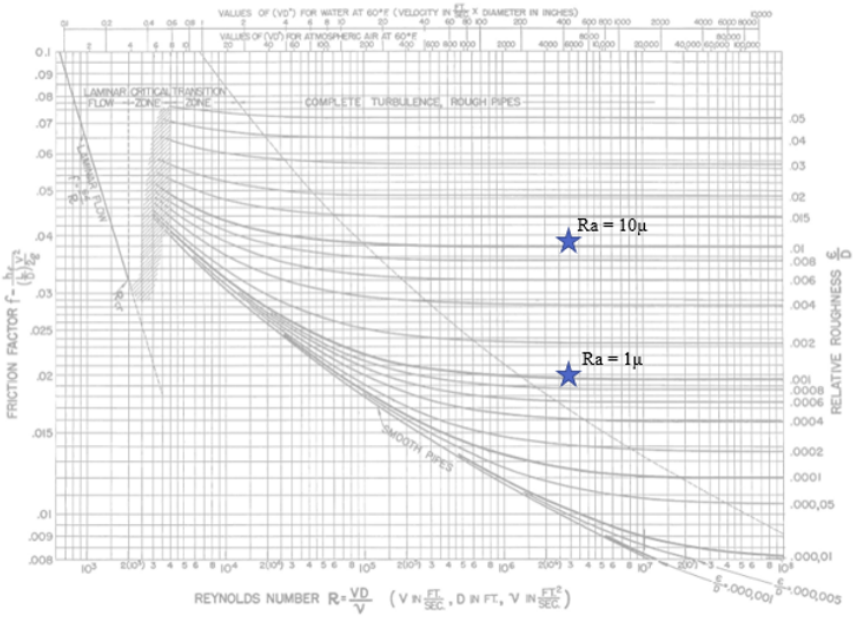

(a) Reynolds number for pipe flow, adapted from Moody [27].

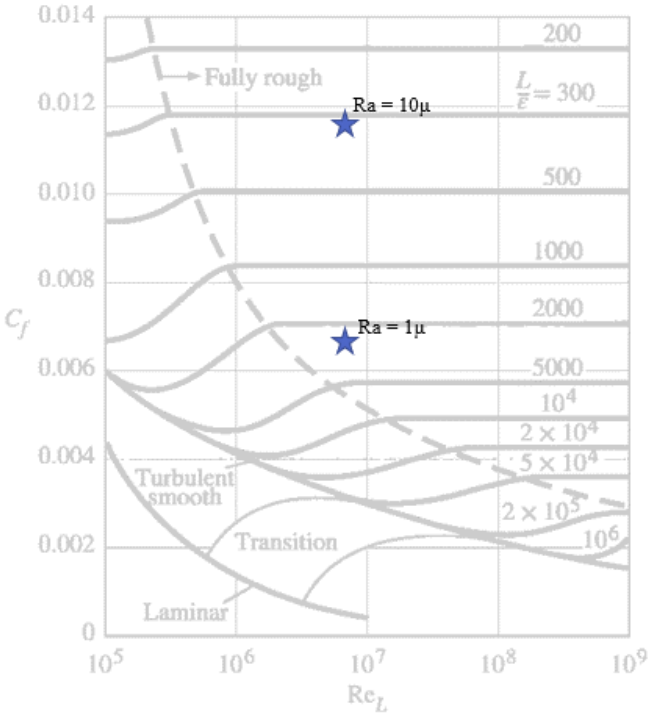

(b) Reynolds number for flat plate flow, adapted from Cengel and Cimbala [28].

Figure 2.7: The small-scale impeller under study operates in the fully turbulent regime for an R_a of 1 and 10 μm.

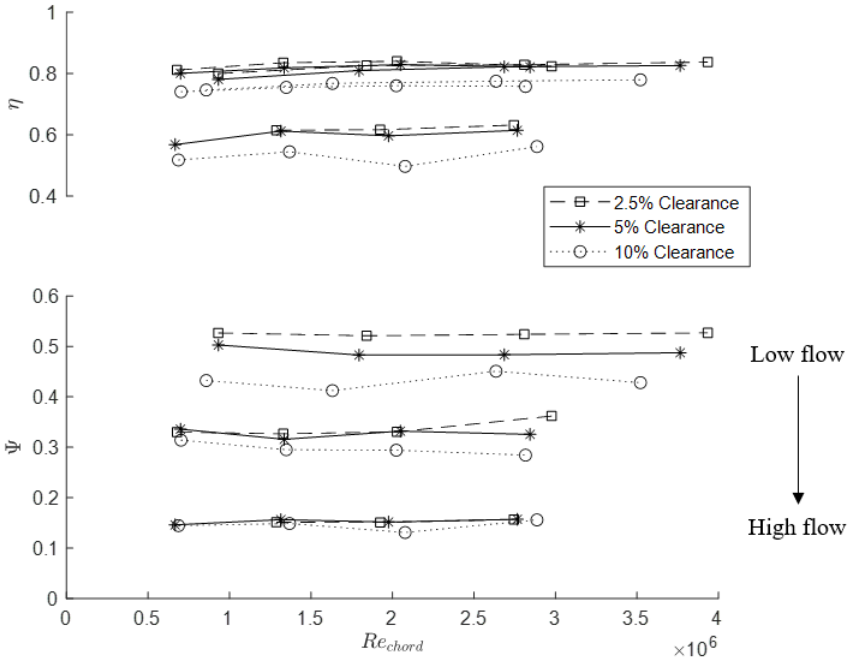

Figure 2.8: Efficiency and head rise are Reynolds number independent for all tested clearances and at three flow coefficients.

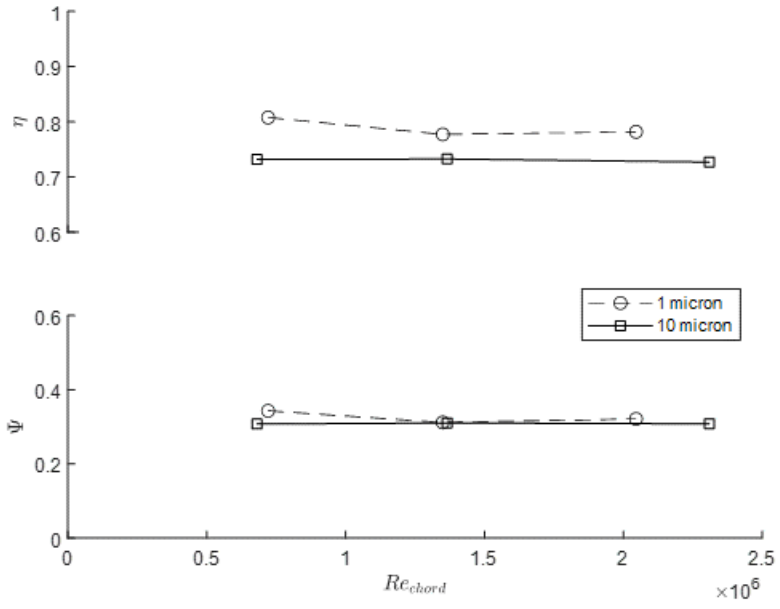

Figure 2.9: Efficiency and head rise are Reynolds number independent for an R_a of 1 and 10 μm at a constant flow coefficient.

Chapter 3

Computational Set-Up

To explore how blade tip clearance and surface roughness affect the performance of small-scale turbopump impellers, three-dimensional Reynolds averaged Navier-Stokes (RANS) simulations were conducted using the commercial software FINE/Turbo. FINE/Turbo incorporates surface roughness by enforcing a minimum wall cell height that is twice the surface roughness parameter, leading to a mesh with high y+ values. Validation of this mesh was achieved through a mesh convergence study and the application of wall functions to resolve the boundary layer. All presented CFD results had less than a 0.1% discrepancy between inlet and outlet mass flow, and resolved global residuals, efficiencies, and pressure rise.

3.1 Channel Geometry

The geometry of the small-scale impeller is illustrated in Figure 3.1 and detailed in Table 3.1. The blade features a blunt leading edge and 0.5mm constant-radius hub fillets. Tip clearance is defined relative to the exit blade span. To reduce computational cost, periodic boundary conditions were applied to a 60° annular section encompassing a single blade (Figure 3.2).

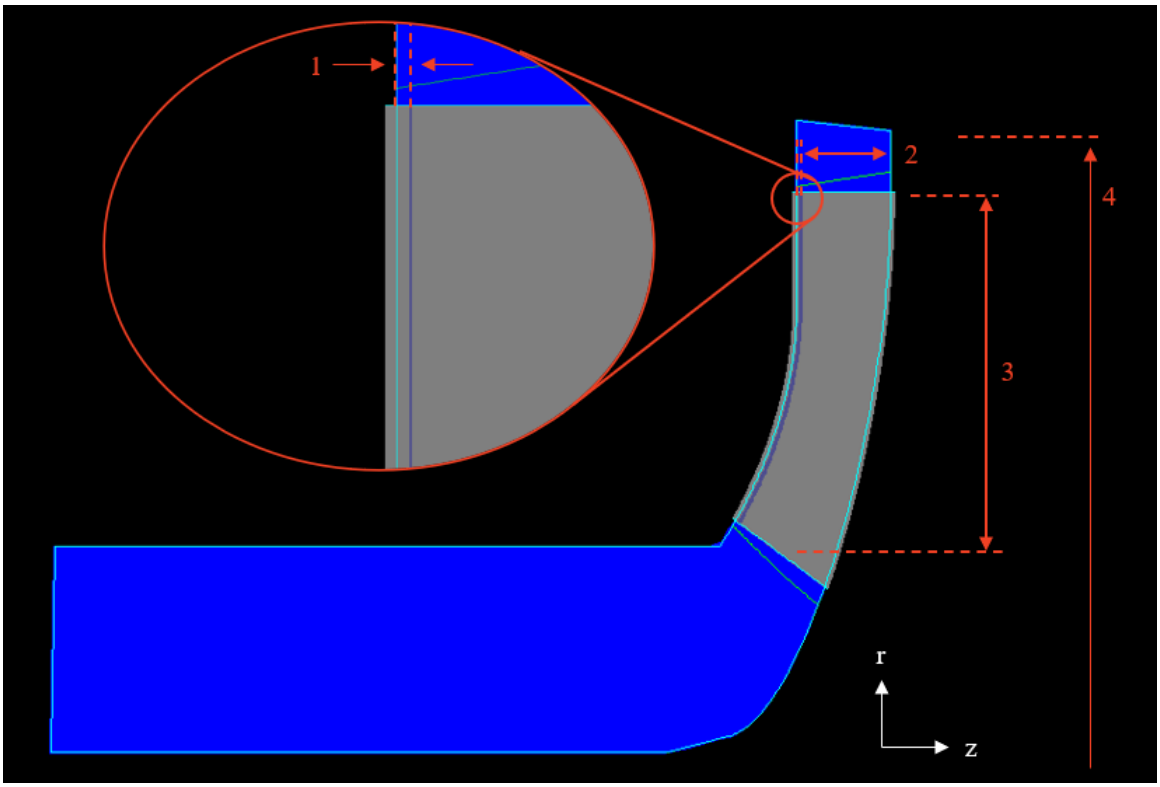

Figure 3.1: Meridional view of flowpath.

	Impeller geometry	Value [cm]
1	Blade tip clearance	6.35e-3, 1.27e-2, 2.54e-2
2	Exit blade span	0.254
3	Blade chord	1.65
4	Impeller diameter	4.4

Table 3.1: Defining geometry values.

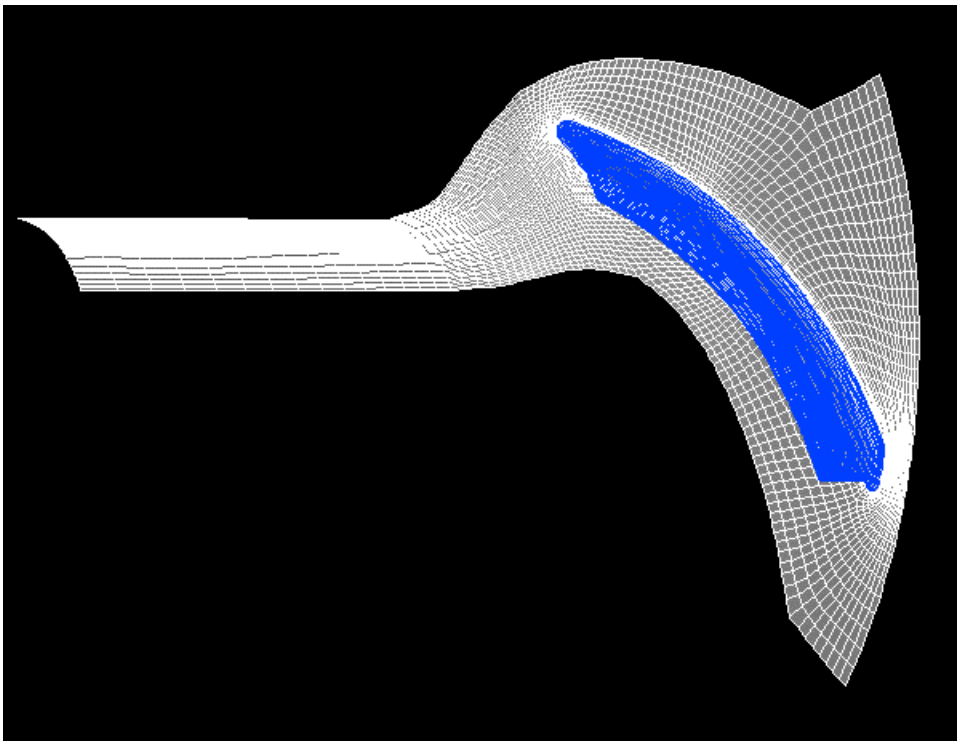

Figure 3.2: Periodic domain reduces the computational cost. The depicted mesh is for the second grid level.

3.2 FINE/Turbo Implementation

Mesh and Turbulence Model

A structured mesh with an O4H topology was selected, comprising an O-block surrounding the blade and four H-blocks along the pressure side, suction side, inlet, and outlet of the blade, as illustrated in Figure 3.3. The mesh was refined to approximately 3 million grid points, as shown in the blade-to-blade view in Figure 3.4. Within the tip clearance gap, the mesh resolution was maintained at 33 cells in the axial direction to ensure grid independence [29]. Throughout all simulations, orthogonality was kept above 20 degrees, the expansion ratio under 3, and the aspect ratio less than 3000.

The Spalart-Allmaras (SA) turbulence model, which is known to have good numerical stability and is suitable at high-pressure conditions [30], was used. The extended wall func-

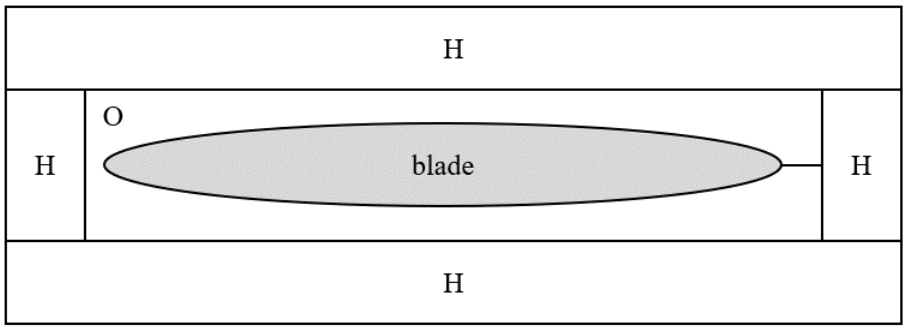

Figure 3.3: O4H topology.

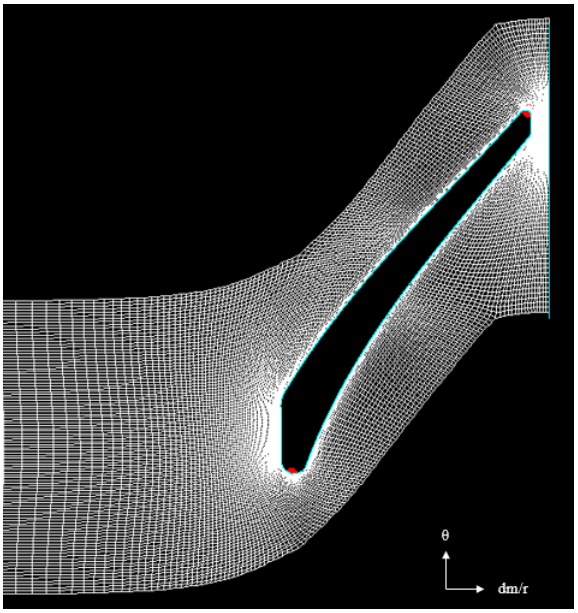

Figure 3.4: Blade-to-blade view of roughly 3 million cells.

tion method was employed due to the high Reynolds number. The general recommendation for high Reynolds flows is to keep the y+ value below 50, though higher y+ values have been shown to provide accurate results when a wall model is applied [31]. The contour plot of the y+ values is shown in Figure 3.5, indicating that most cells fall within the recommended range. Higher y+ values are caused by the way FINE/Turbo incorporates surface roughness in that the minimum wall cell height must be at least twice the FINE/Turbo roughness parameter $k0 \approx R_a/5$. Since this study focused on the bulk flow features rather than boundary layer behavior, this lower boundary layer resolution was acceptable. Figure 3.6 shows a mesh convergence analysis of percent error in mass flow rate and node count.

When determining the acceptability of the mesh, greater emphasis was placed on achieving mesh convergence over maintaining a specific y+ value. Turbulent viscosity was determined based on the values recommended by Numeca for turbomachinery flows [31].

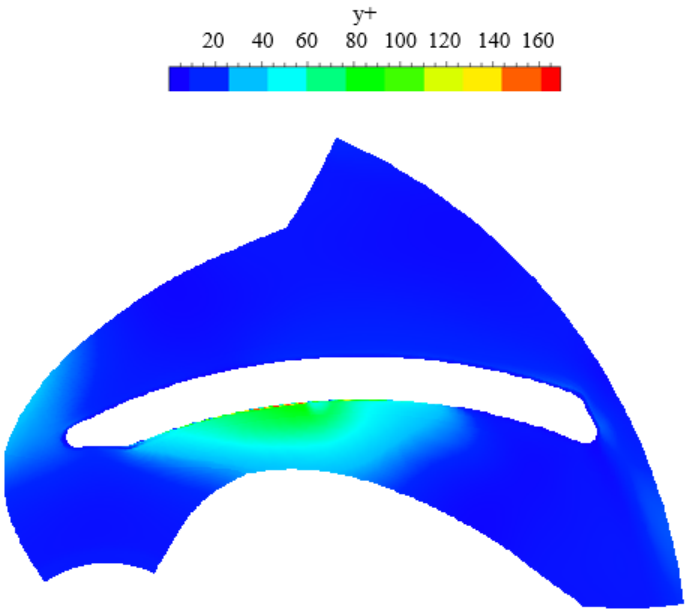

Figure 3.5: Higher y+ values result from wall cell height requirements for rough surfaces in FINE/Turbo.

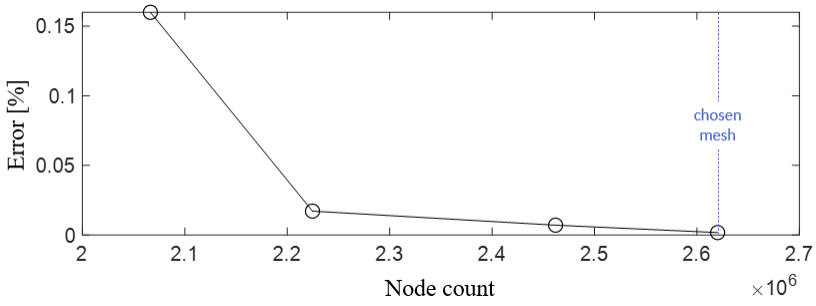

Figure 3.6: Mesh convergence despite high y+ values provides confidence in mesh quality.

Solver Inputs and Convergence Criteria

Interpolated National Institute of Standards and Technology (NIST) tables were used to determine the thermodynamic properties of liquid methane at 120K and 0.4 MPa. Inlet

boundary conditions were specified by total pressure, total temperature, and zero inlet flow, while outlet boundary conditions were set by static pressure. Wall boundaries were defined as no-slip and adiabatic.

Convergence was assessed based on several criteria including the FINE/Turbo global residual, resolved efficiency and pressure rise values, and a discrepancy between inlet and outlet mass flow below 0.1%. Convergence was typically achieved within 1500 iterations at the finest grid level. However, operating points with lower mass flow rates exhibited oscillating convergence, suggesting unsteady flow, and were therefore not deemed converged despite meeting the convergence criteria.

Chapter 4

Modeling Approach

To assess the impact of blade tip leakage flow, the Storer-Cumpsty jet in cross-flow model was applied. The 3D flow field from the computation was averaged appropriately to provide the required inputs to the control volume analysis. To compare the Storer-Cumpsty model with the 3D computation, the non-uniform flow at the impeller exit is mixed out. This introduces an additional loss of 4% to 6%. The 3D computation was averaged to extract the input parameters for the Storer-Cumpsty model.

4.1 Storer-Cumpsty Model

A control volume for an axial compressor posited by Storer and Cumpsty [7] models blade tip leakage flow as a jet being injected into the cross-flow within the passage. This jet in cross-flow model was used to estimate contributions of the blade tip leakage flow to overall loss for the small-scale impeller in this study.

As shown in Figure 4.1a, a schematic adapted from Greitzer [32], the control volume (delineated by dotted lines) encompasses the mixing region between the jet and cross-flow. The input parameters for the control volume include geometry, the jet injection angle (α) and the areas of the jet and passageway, as well as flow properties, static pressure (P) and velocity (u), for both the jet and the main flows. To avoid back flow, the static pressure of

the jet must be greater than or equal to the static pressure at the inlet of the main flow. This assumption is reflected in the inlet boundary conditions depicted in Figure 4.1b.

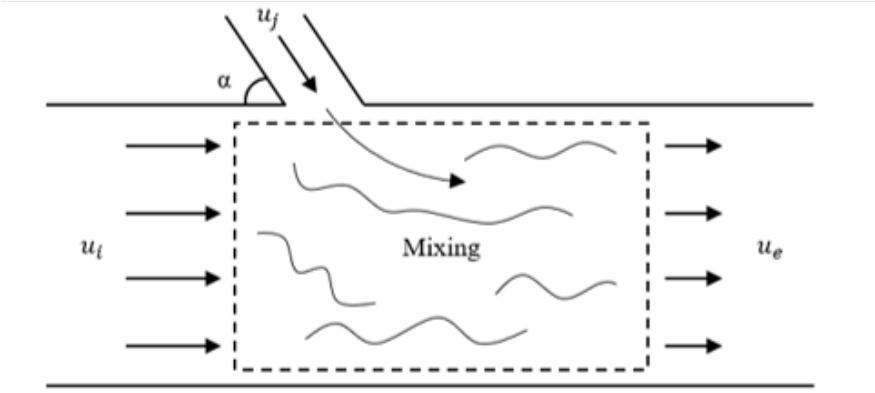

(a) Storer-Cumpsty model

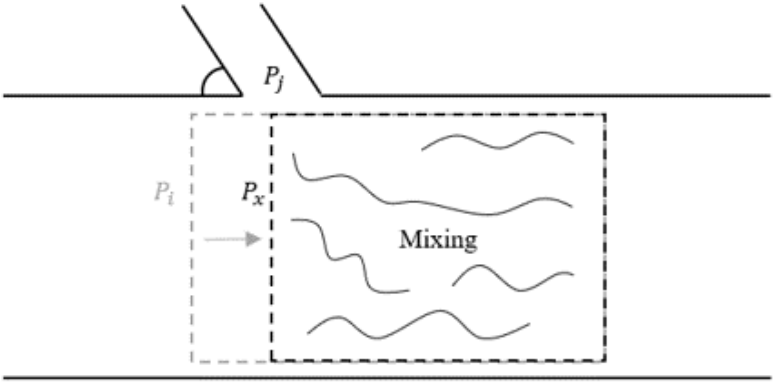

(b) Control volume for this thesis

Figure 4.1: The Storer-Cumpsty model is adjusted to avoid back flow.

In this study, constant area mixing is applied. The jet is defined using ratios for mass flow rate, area, and stagnation pressure based on main passage inlet conditions at the operating point with the flow coefficient (ϕ) equal to 0.2.

The three ratios defining the jet parameters were varied along with the injection angle. By applying continuity (Equation 4.1) and conservation of momentum (Equation 4.2), the fully mixed out properties were obtained.

$$u_e = u_i \frac{A_i}{A_e} + u_j \frac{A_j}{A_e} \tag{4.1}$$

$$P_{s,o} = P_{s,i} \frac{A_i}{A_e} + \rho({u_i}^2 \frac{A_i}{A_e} + {u_j}^2 \cos\alpha \frac{A_j}{A_e} - {u_e}^2) \tag{4.2}$$

The stagnation pressure loss, as defined in Equation 4.3, is determined based on the weighted stagnation pressure of the two streams at the inlet. This provides a more representative measure of overall loss by considering the jet contribution, which originates from the passage flow of the previous blade.

$$Loss = \frac{\frac{(\dot{m}_i P_{t,i} + \dot{m}_j P_{t,j})}{\dot{m}_i + \dot{m}_j} - P_{t,o}}{0.5\rho {u_o}^2} \tag{4.3}$$

4.2 Averaging

Cumpsty details various methods for averaging non-uniform flows to obtain the exit stagnation pressure and loss [33]. The choice of averaging method depends on the specific purpose of the analysis. In this research, three averaging methods are employed: area averaging for static pressure, mass averaging for stagnation pressure, and mixed-out averaging for obtaining uniform flow properties.

4.2.1 Fully Mixed Impeller Outflow

The exit flow of the small-scale impeller throughflow estimated by CFD must be mixed out to compare with the Storer-Cumpsty model. The additional loss from mixing to uniform flow is subtracted from the control volume analysis to estimate the contribution to overall loss from blade tip leakage flow.

Mixed-out averaging was used to calculate the exit stagnation pressure by mass-averaging the individual inlet properties and then applying conservation equations to determine the

exit properties. Constant area mixing was applied to be consistent with the assumptions used in the Storer-Cumpsty model. An alternative method for estimating mixing is provided in Appendix A.

Flow is expected to fully mix out within five diameters of the larger passageway [32]. In turbopumps, the impeller outflow exits with high tangential velocity, resulting in distances traversed in the volute exceeding five diameters. Therefore, the loss from mixing out is important to consider when calculating overall loss.

Implementation of the Mixed Out Average

The control volume for mixed-out averaging is depicted in Figure 4.2. Point i represents the exit plane of the computation. The control volume inputs are comprised of velocity and static pressure values at each grid node on the exit plane. The outlet properties, including averaged velocity and pressures, were determined by solving the continuity (Equation 4.4) and the conservation of momentum equations (Equation 4.5).

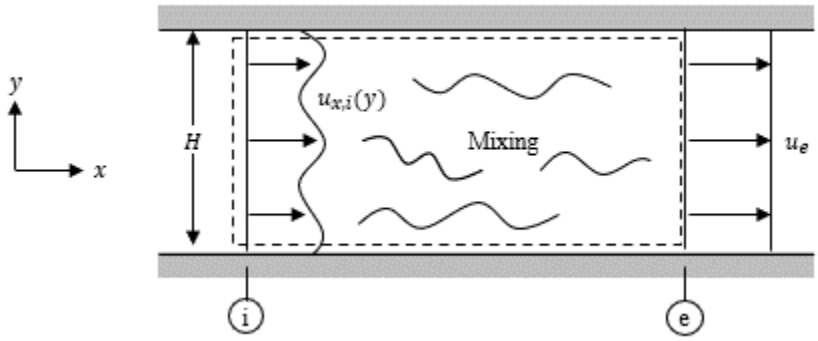

Figure 4.2: Control volume determines mixing loss.

$$\int_0^H u_{x,i}\, dy \;= \bar{u}\, H \tag{4.4}$$

$$\int_0^H (P_i + \rho\, u_{x,i}^2)\, dy \;= (P_e + \rho\, \bar{u}^2)\, H \tag{4.5}$$

Over a constant flow rate, the additional loss from mixing out varies over clearance case between 4% for 2.5% clearance, and 6% for 10% clearance.

4.2.2 Obtaining Model Parameters from Computational Results

Using the jet in cross-flow model necessitates the parameters for both the main flow and the jet flow to appropriately map the CFD onto the control volume model. For the main flow, non-dimensional parameters were derived from the bulk flow characteristics at the inlet to the impeller, while for the jet flow, these parameters were based on local flow properties in the tip gap along the blade chord.

Main Flow

Inlet conditions for the main flow are calculated by averaging the flow properties prior to entry into the impeller. The inlet cross-flow plane is visualized in Figure 4.3. Aggregate parameters were calculated using mass averages, an example for stagnation pressure is shown in Equation 4.6.

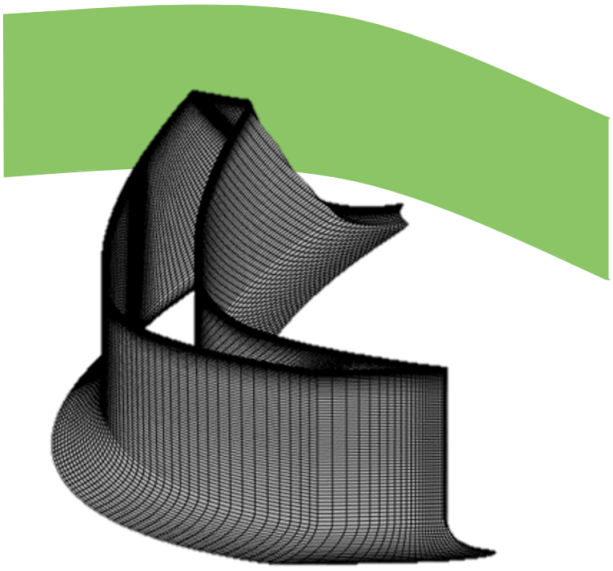

Figure 4.3: Plane over which main inlet flow properties are averaged.

$$P_{t,i} = \frac{\iint_A (P + \frac{1}{2}\rho w^2)\rho w_n \, dA}{\iint_A \rho w_n \, dA} \tag{4.6}$$

Jet flow

The methodology for determining inlet conditions for the jet flow mirrors that of the main flow, utilizing the same equations and computational techniques. However, the jet properties necessitate an assessment throughout the passageway as blade tip leakage flow properties change along the chord. Defining the jet parameters for the control volume in this way captures how the jet changes through the impeller, and thus characterizes overall jet behavior.

The determination of the jet properties focused on the blade loading near the tip clearance along the blade camber. Blade loading in impellers is a critical parameter that describes the pressure distribution across the blade surface, from the leading edge to the trailing edge. This parameter is derived from the pressure differential between the pressure side and the suction side of the blade. For the jet flow, the inlet plane is defined as the plane that follows the suction side of the clearance gap, as illustrated in Figure 4.4.

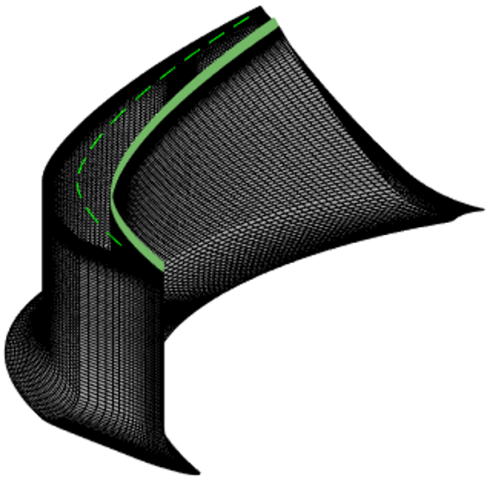

Figure 4.4: Camber line, and the plane over which jet inlet flow properties are averaged.

The last input parameter needed for the control volume analysis is that of the injection angle, α. The injection angle is defined as the angle between the velocity vector of the jet

flow and the camber line of the blade. The camber line was defined by the suction and pressure edges of the blade and is illustrated by the dashed green line in Figure 4.4. To compute the mass-averaged injection angle, the velocity vectors at discrete points on the inlet plane were resolved relative to the camber line, and the resulting angles were weighted by the local mass flow.

As the tip clearance decreases, the injection angle from the inlet to the outlet exhibits greater variation. This is because the blade tip leakage flow in smaller tip clearances has less momentum and thus less resistance to turning. The average angle between the pressure and suction side of the blade is illustrated in Figure 4.5. 2.5% tip clearance changes by 20° while 10% clearance stays within 5° along the blade length. The trends seen in Figure 4.5 underscore the necessity of defining the jet characteristics by examining the internal flow field rather than relying solely on a local jet angle. Sampling at a single cross-flow plane would lead to an incorrect injection angle for lower clearances.

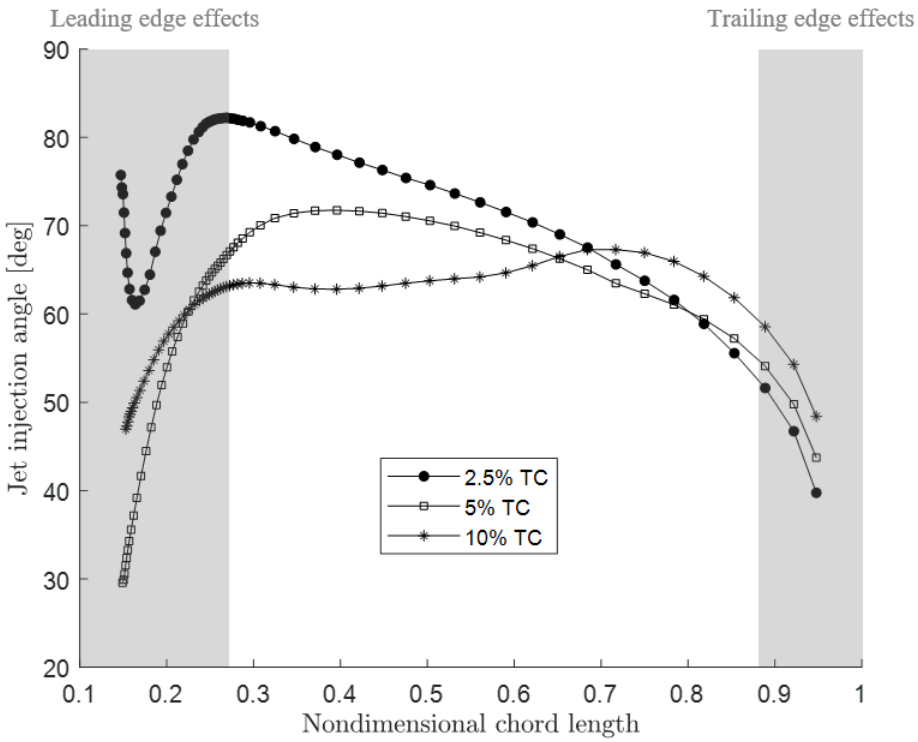

Figure 4.5: Injection angle has higher variation as tip clearance decreases.

The averaged results of the jet and main flow parameters are expressed as the ratios needed to define the jet in cross-flow control volume, and presented in Table 4.1. Mass flow ratio scales with tip clearance.

	2.5% Tip clearance	5% Tip clearance	10% Tip clearance
P_t Ratio	1.10	1.11	1.10
$\dot{m}$ Ratio	0.05	0.1	0.2
α [deg]	69	63	64

Table 4.1: Averaged inlet property ratios for Storer-Cumpsty model.

Chapter 5

Effects of Tip Clearance on Impeller Performance

This chapter demonstrates the two main flow features are the blade tip leakage flow and secondary flow consequence of streamwise vorticity. The blade tip leakage flow contributes over 80% of loss in the impeller at higher clearances, and the loss from the blade tip flow is not impacted by the number of blades over which the blade tip jet flows before mixing with the passage flow. As blade tip clearance decreases, the secondary flow loss increases while the loss from blade tip leakage decreases. At 2.5% blade tip clearance, both flow features contribute equally to the overall loss. This increased influence of a leading-edge vortex, which is absent at higher tip clearances, increases secondary loss at low tip clearances. Consequently, this flow feature separates the flow field into two distinct regimes: one with high tip clearance, where losses are predominantly due to blade tip leakage, and another with low tip clearance, where half of loss is from secondary flow and the other half is from blade tip leakage. The estimated contribution to total loss from the leading-edge vortex is 25% for the 2.5% clearance case.

To separate tip clearance effects from roughness effects, computations were first run with smooth walls. At a constant Reynolds number of 1.5 million, tip clearance was varied

from 2.5% to 10% of the exit blade span. The comparison of flow fields between blade tip clearances are at a ϕ of 0.2.

5.1 Performance Summary for Varied Blade Tip Clearances

The characteristics for 2.5% and 10% blade tip clearance are plotted against the baseline 5% clearance case for smooth wall simulations. Figure 5.1 shows decreases in efficiency and head rise with increasing clearance.

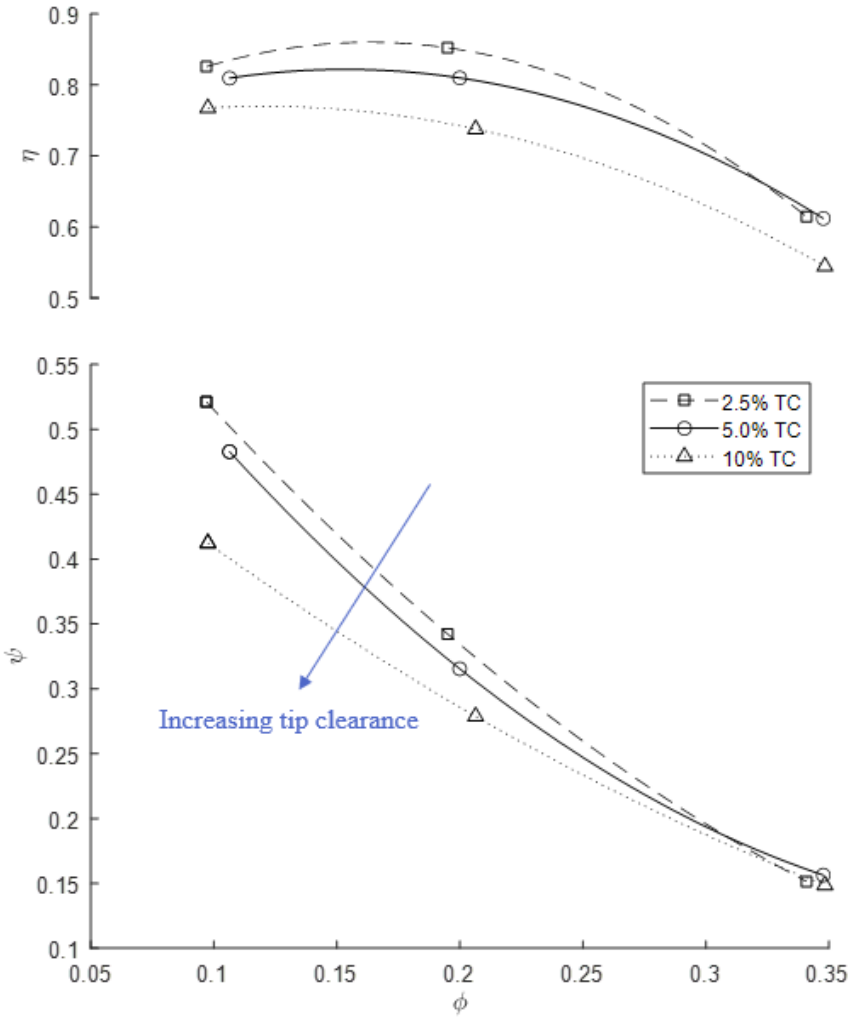

Figure 5.1: Maximum efficiency for the small-scale impeller under study is at a ϕ of 0.15.

Pitch-wise averaged meridional plots for the flow field of the baseline 5% blade tip clearance with smooth surfaces simulation are provided in Figures 5.2 to 5.4 for the operating points at a ϕ equal to 0.2. At the same ϕ, comparisons between performance for the blade tip clearances analyzed are shown in Figures 5.5 to 5.7. The flow coefficient is defined as $\phi = \frac{w_m}{U}$, stagnation pressure coefficient as $c_{p_t} = \frac{P_t - P_{t_0}}{\rho U^2}$, and static pressure coefficient as $c_p = \frac{P_s - P_{s_0}}{\rho U^2}$.

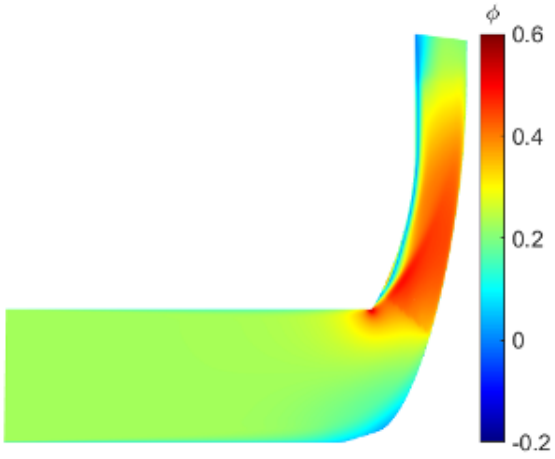

Figure 5.2: Flow coefficient for the baseline 5% blade tip clearance, smooth surface simulation at a $\phi = 0.2$.

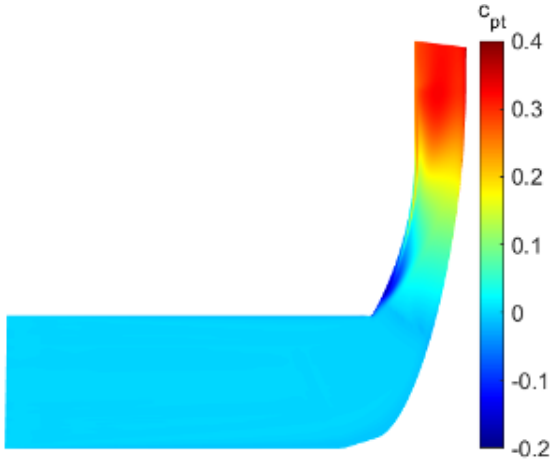

Figure 5.3: P_t coefficient for the baseline 5% blade tip clearance, smooth surface simulation at a $\phi = 0.2$.

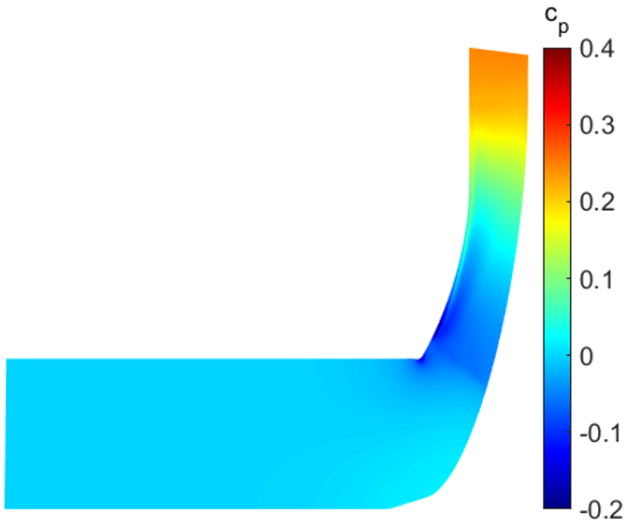

Figure 5.4: P_s coefficient for the baseline 5% blade tip clearance, smooth surface simulation at a $\phi = 0.2$.

(a) 2.5% Clearance (b) 5% Clearance (c) 10% Clearance

Figure 5.5: Larger region of low meridional velocity in the tip gap with increasing clearance at a $\phi = 0.2$.

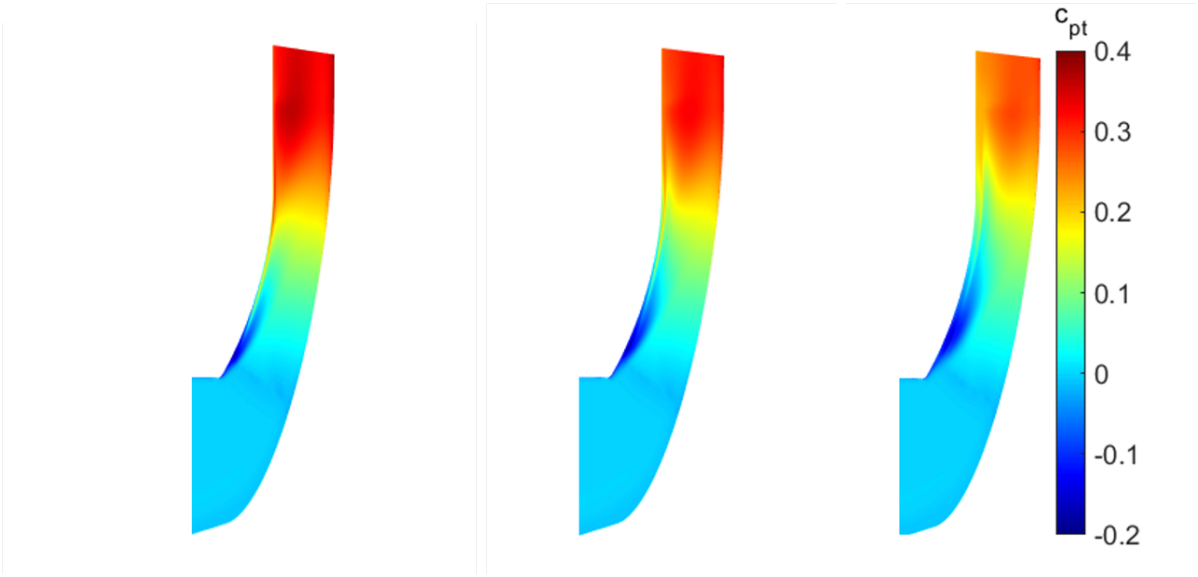

(a) 2.5% Clearance (b) 5% Clearance (c) 10% Clearance

Figure 5.6: Lower exit stagnation pressure with increasing tip clearance at a $\phi = 0.2$.

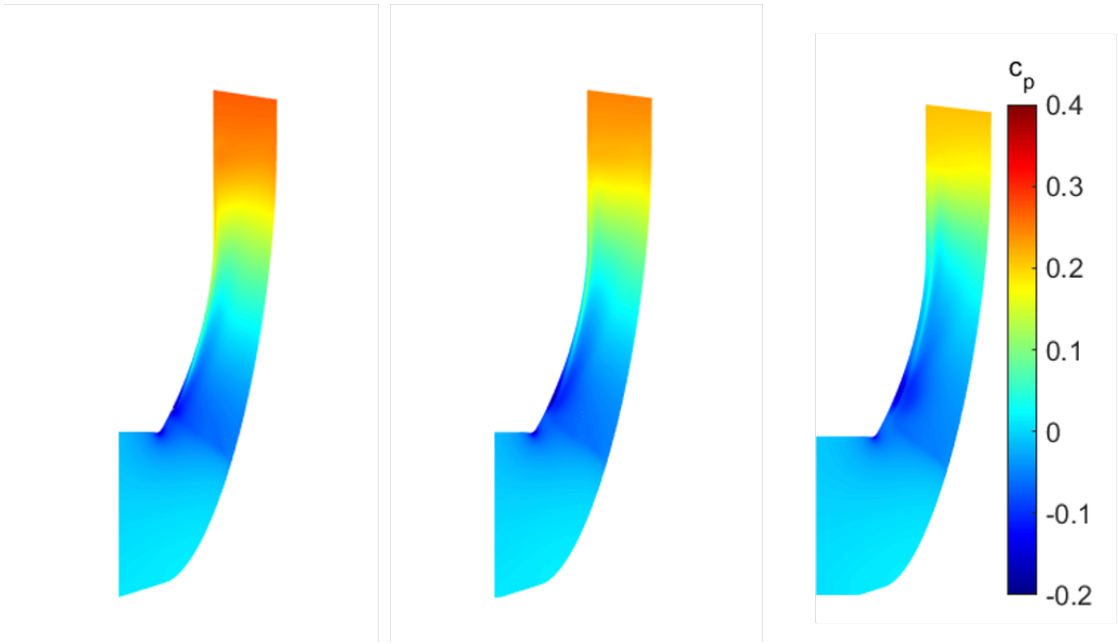

(a) 2.5% Clearance (b) 5% Clearance (c) 10% Clearance

Figure 5.7: Lower exit static pressure with increasing tip clearance at a $\phi = 0.2$.

5.2 Effects of Blade Tip Leakage Flow on Impeller Performance

The blade tip leakage flow originates from flow moving up the pressure side of the blade then through the tip clearance gap. At the suction side corner of the blade, a vortex sheet at the interface between the passage flow and blade tip leakage flow rolls up to form a tip leakage vortex, which then mixes with the main flow down the impeller passage. Loss due to the mixing between the two flows is illustrated in Figure 5.8 and defined in Equation 5.1.

$$s^* = \frac{T_t \, \Delta s}{\frac{1}{2} U^2} \tag{5.1}$$

Relative velocity streamlines originating from the tip gap are superimposed on cross-stream contour plots at constant radii along the blade passage. It can be seen that regions of high loss are due to the blade tip leakage flow mixing with the main flow. As blade tip clearance increases, the blade tip leakage vortex grows and increases overall impeller loss.

The estimated contributions to overall loss of the blade tip leakage using the Storer-Cumpsty model are 49%, 82%, and 88% for 2.5%, 5%, and 10% clearance, respectively, as illustrated in Figures 5.9 to 5.11 and in Table 5.1. The red star represents the jet injection angle and mass flow ratio to the control volume from 4.1, with the corresponding control volume loss estimation represented by the solid red line. Computational results of the total loss are depicted by the dashed red line. The contour line representing the total loss is not seen on Figure 5.9 because, at the given control volume parameters, the model cannot reach losses that high with just blade tip leakage flow loss.

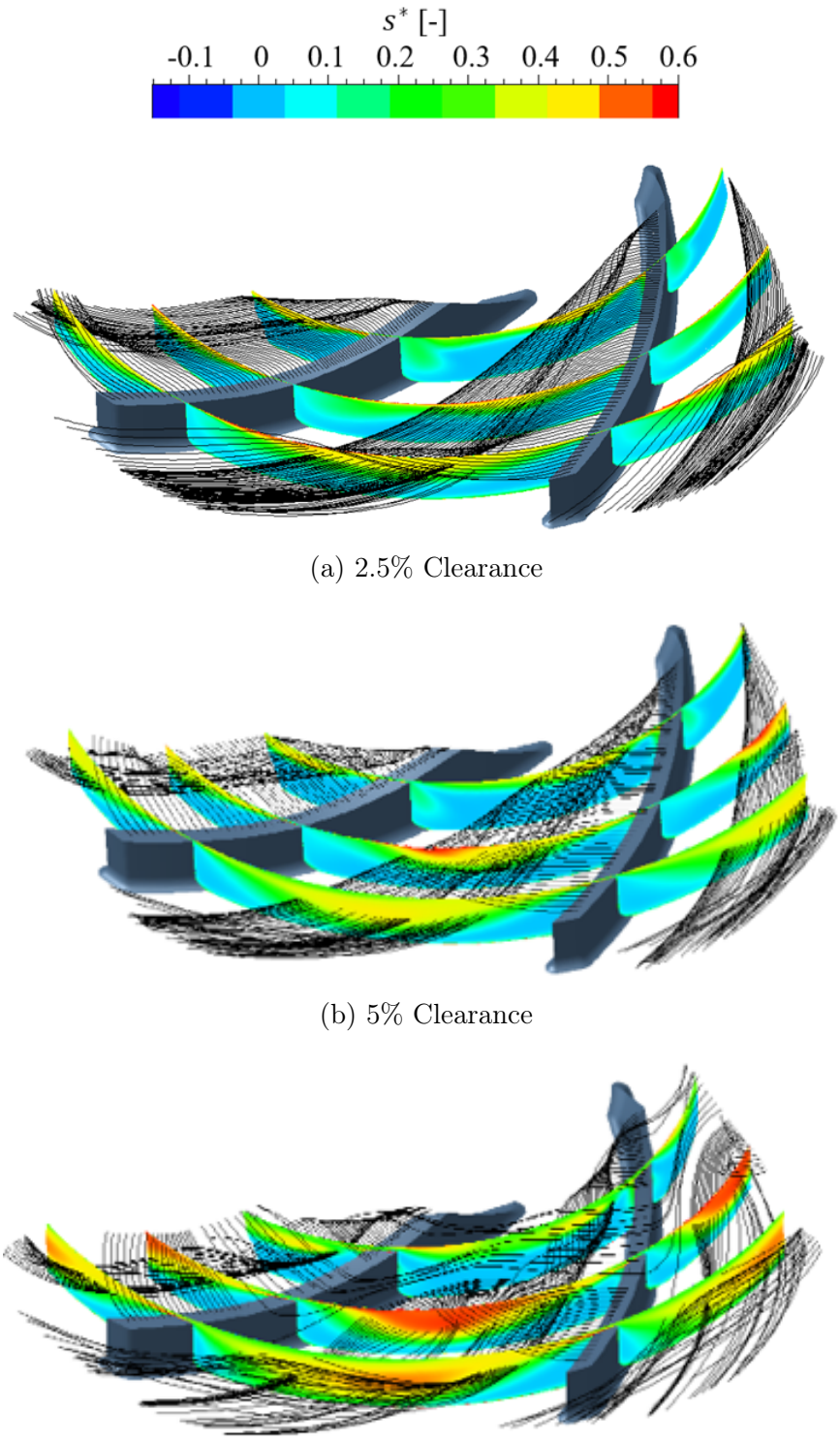

(a) 2.5% Clearance

(b) 5% Clearance

(c) 10% Clearance

Figure 5.8: Mixing of blade tip leakage flow is the primary source of loss at $\phi = 0.2$.

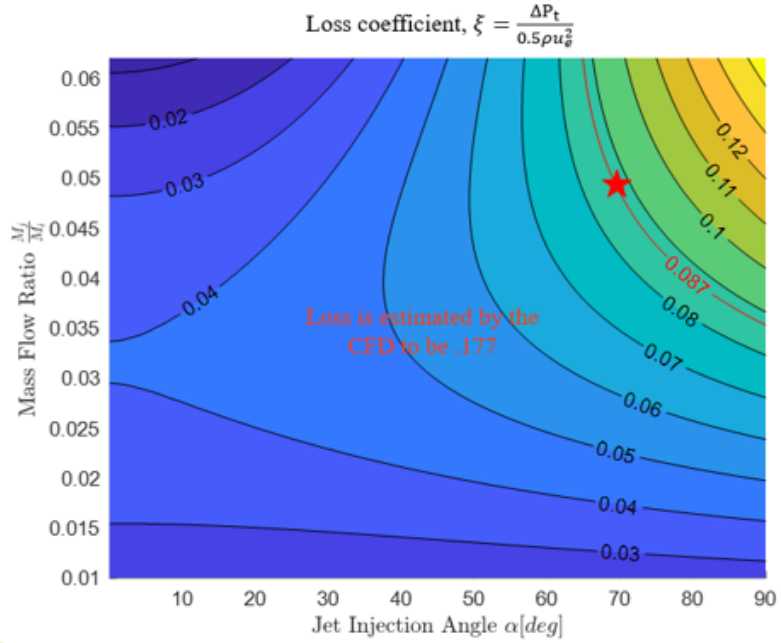

Figure 5.9: For 2.5% clearance at a ϕ of 0.2, blade tip leakage flow mixing with the passage flow is estimated to cause an 8.7% drop in efficiency. Computations estimate overall impeller loss to be 17.7%, indicating about half of this loss is attributed to blade tip leakage flow.

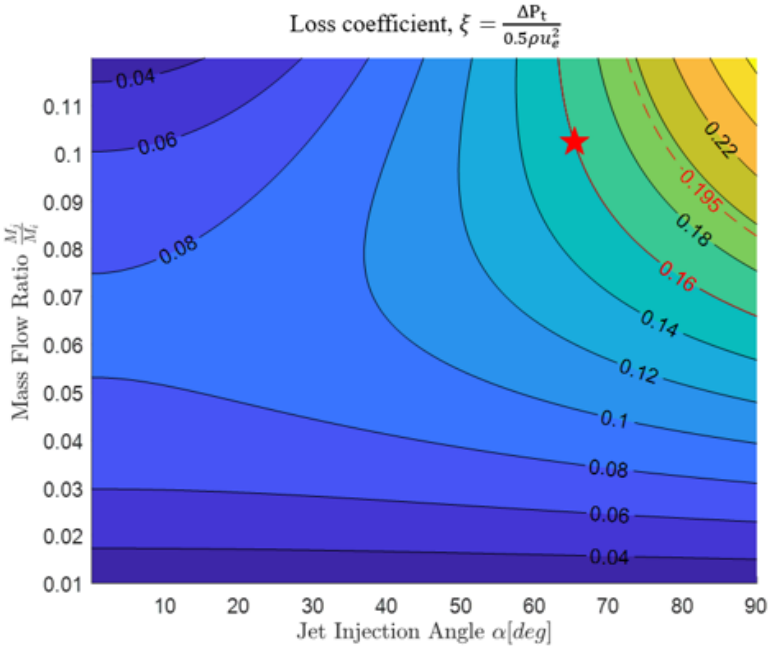

Figure 5.10: For 5% clearance at a ϕ of 0.2, blade tip leakage flow mixing with the passage flow is estimated to cause an 16% drop in efficiency. Computations estimate overall impeller loss to be 19.5%, indicating 82% of this loss is attributed to blade tip leakage flow.

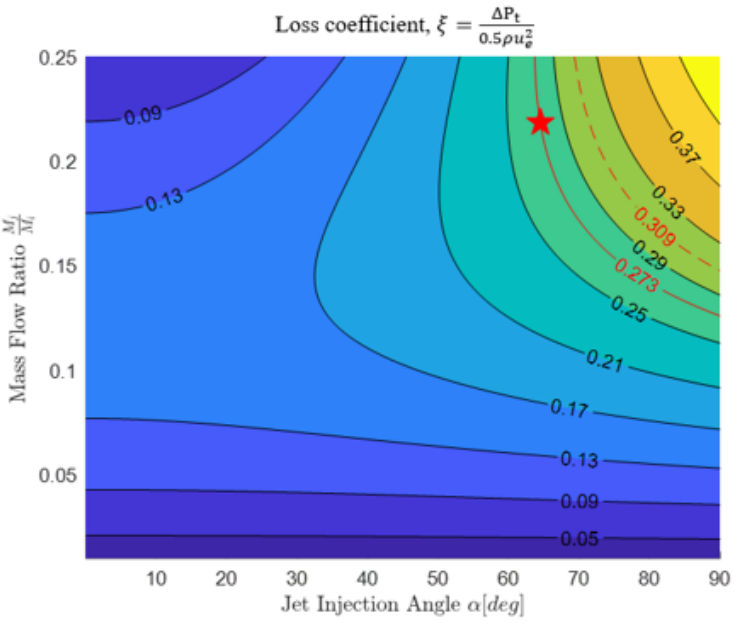

Figure 5.11: For 10% clearance at a ϕ of 0.2, blade tip leakage flow mixing with the passage flow is estimated to cause an 30.9% drop in efficiency. Computations estimate overall impeller loss to be 12.3%, indicating 88% of this loss is attributed to blade tip leakage flow.

Loss calculation	2.5% Clearance	5% Clearance	10% Clearance
Overall (computation)	17.7%	19.5%	30.9%
Blade tip leakage (model)	8.7% *(49.2%)*	16.0% *(82.1%)*	27.3% *(88.3%)*

Table 5.1: Mixing from blade tip leakage flow is the dominant source of loss for smooth surfaces. Percentages in parentheses are contribution of blade tip leakage loss to overall loss.

For 5% and 10% blade tip clearance, some blade leakage streamlines tangentially traverse the impeller, staying about the blade tip leakage vortex, then flow over the subsequent blade before they mix with the flow in the adjacent passage. This phenomenon, termed "double" blade tip leakage, is highlighted in Figure 5.12 for a ϕ of 0.2, though it is also present at all flow rates for 5% and 10% tip clearances. Double blade tip leakage is not present for the 2.5% clearance case because the entirety of the blade tip leakage flow mixes with the blade tip leakage vortex. There is little entropy rise along double blade tip leakage streamlines

until mixing with the passage flow, indicating that it does not significantly alter the total loss compared to if all the blade tip leakage flow were mixed directly after passing over a single blade.

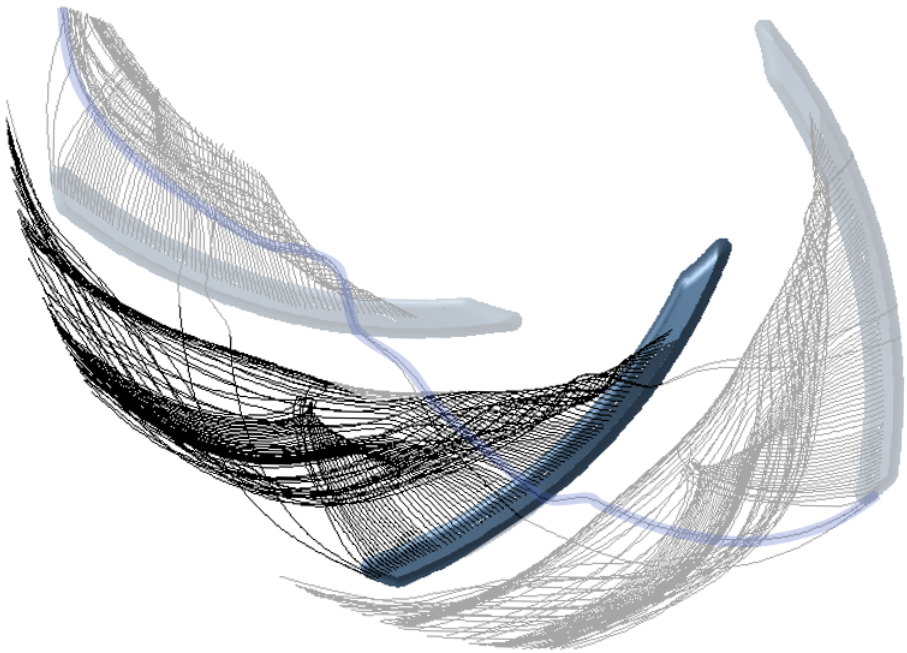

Figure 5.12: Double blade tip leakage flows over multiple blades before mixing into the main stream for 10% tip clearance at $\phi = 0.2$.

The radial pressure gradient through the flow field causes streamlines leaving the impeller to curve upstream against the bulk flow. The phenomenon is called backflow, and occurs for all three blade tip clearances and at all flow rates computed. Figure 5.13 illustrates a single relative velocity streamline for 5% tip clearance that, after exiting the impeller, reenters the passage at the suction side of the trailing edge of the blade as this is where the radial pressure gradient is highest. The streamlines associated with backflow become blade tip clearance flow and mix in with the passage flow, increasing the overall loss in the impeller.

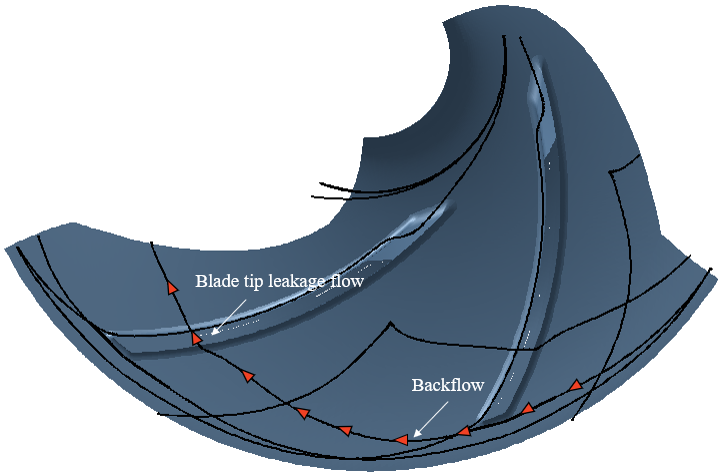

Figure 5.13: Backflow increases the mass flow of blade tip leakage. Plotted is 5% tip clearance at a $\phi = 0.2$.

5.3 Effects of Secondary Flow on Impeller Performance

Secondary flow arises from the tipping of the hub boundary layer vortex into the flow. At the inflow to the passageway, the hub boundary layer vortex lines run across the passageway normal to the flow. As the fluid in the hub boundary layer experiences the same pressure gradient as the main flow but at a lower velocity, the hub boundary layer vortex lines are tipped in a direction parallel to the main flow. In an impeller, the hub boundary layer vortex lines drift toward the suction side of the blade as the passageway curves [32]. As a result, the passage flow moves up the suction side of the blade (Figure 5.14).

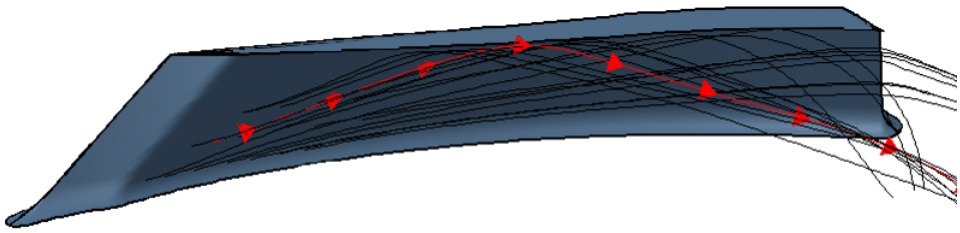

Figure 5.14: Relative streamlines show how flow moves up along the suction side of the blade as a result of the hub boundary layer vortex tipping into the flow.

When the hub boundary layer vortex meets the leading edge of the blade, it bends into

the flow and creates the leading-edge vortex. The leading-edge vortex is shown for the three blade tip clearances in Figure 5.15. In the 5% and 10% tip clearance cases, the blade tip leakage flow carries the leading-edge vortex through the tip clearance gap. Consequently, blade tip leakage flow remains the dominant flow feature for all flow rates simulated. For 2.5% tip clearance, where blade tip leakage flow is half that of 5% clearance, the leading-edge vortex is carries by the main flow down the passageway. The loss due to the leading-edge vortex for the 2.5% tip clearance case can be seen in Figure 5.16.

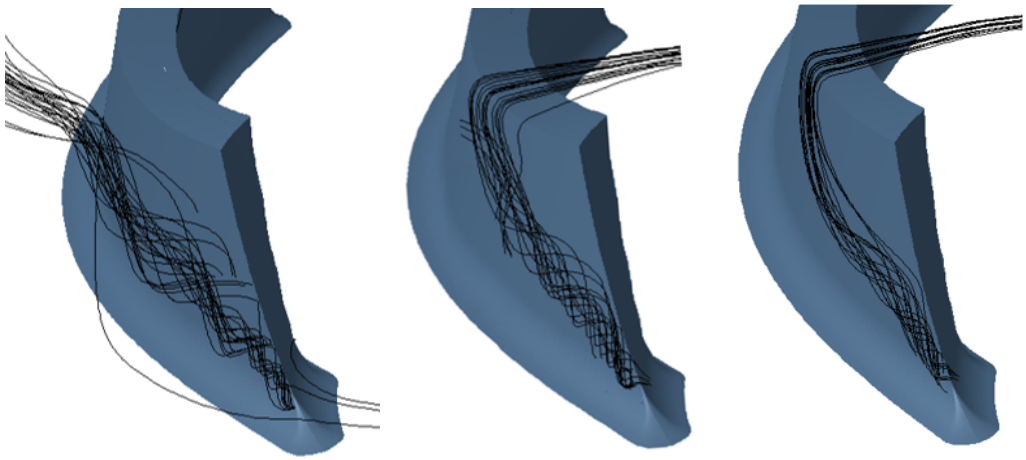

(a) 2.5% Clearance (b) 5% Clearance (c) 10% Clearance

Figure 5.15: Leading-edge vortex turns to blade tip leakage flow for 5% and 10% tip clearance at $\phi = 0.2$.

Relative streamlines composing the leading-edge vortex move up and away from the pressure side of the blade, and can be explained through fictitious image vortices. In the relative frame, the blade walls are stationary and therefore the relative leading-edge vortex lines cannot end on a boundary surface because of the no-slip condition at the wall. Applying the concept of image vortices to the interaction between the blade pressure side and the leading-edge vortex shows how the leading-edge vortex moves up the blade span. Figure 5.17 shows a schematic adapted from Greitzer [32] illustrating the movement of the leading-edge vortex. For 2.5% tip clearance, where the blade tip leakage flow does not carry the leading-edge vortex through the clearance gap, the pressure gradient across the passageway pulls the leading-edge vortex away from the pressure side of the blade.

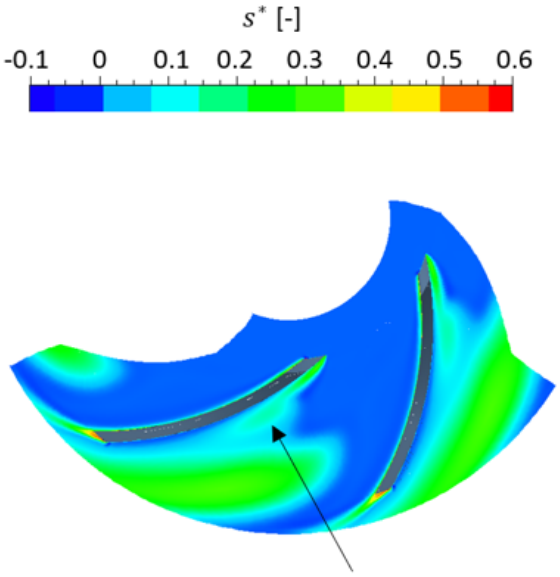

(a) 2.5% Clearance

(b) 5% Clearance

(c) 10% Clearance

Figure 5.16: Formation of the leading-edge vortex that causes secondary flow is seen for the 2.5% tip clearance case. Contour plots are at 50% of the blade span and a $\phi = 0.2$.

Figure 5.17: Image vortices explain leading-edge vortex streamlines moving counter to secondary flow.

To estimate the contribution to overall loss from the leading-edge vortex, the mass-averaged entropy rise was calculated along streamlines classified as either blade tip leakage flow, leading-edge vortex, or main flow. Streamlines were released from the uniform flow impeller inlet. Those composing the blade tip leakage flow were readily identifiable by their passage through the clearance gap. In contrast, distinguishing leading-edge vortex streamlines from main passage streamlines proved challenging as the leading-edge vortex influenced adjacent streamlines which obscured clear categorization. The streamlines chosen to define the leading-edge vortex were those involved since its formation. Streamlines influenced by the leading-edge vortex were categorized within the main flow. Recognizing that doing so would lead to a substantial portion of the effects of the leading-edge vortex would be categorized within the main flow, the leading-edge vortex was estimated to account for at minimum 25% of the total impeller loss for a ϕ of 0.2. The breakdown of streamline contributions is detailed in Table 5.2.

	Leading-edge vortex	Blade tip leakage flow	Main flow
Streamline distribution	6%	8%	86%
Contribution to loss	25.1%	55.0%	19.9%

Table 5.2: For 2.5% tip clearance, at least 25% of overall impeller loss comes from the leading-edge vortex for $\phi = 0.2$. Blade tip leakage flow is estimated to contribute 55% of overall loss, a similar estimate as the Storer-Cumpsty model.

Chapter 6

Effects of Roughness on Impeller Performance

At the same Reynolds number used in the tip clearance investigation, two simulations with average surface roughness R_a of 1 μm and 10 μm were compared against the baseline smooth surface simulation. Increased roughness affects the impeller by reducing the effects of blade tip leakage flow, and through stronger secondary flow from a stronger hub boundary vortex.

The impact blade tip leakage flow has on overall impeller loss is reduced by a smaller vena contracta height and a thicker viscous layer within the tip gap. Comparing smooth surfaces to those with a 10 μm roughness at the ϕ with maximum efficiency, the contribution of blade tip leakage to total loss is estimated to decrease by 35% for a 2.5% tip clearance, by 46% for a 5% tip clearance, and by 32% for a 10% tip clearance. Additionally, with the reduced impact of the blade tip leakage flow due to surface roughness, the tip clearance that distinguishes the low clearance and high clearance flow field regimes decreases.

Rougher surfaces subjected to a pressure gradient diffuse more vorticity, thereby strengthening secondary flow. A stronger secondary flow causes the blade tip leakage flow to travel further across the passage before mixing with the main stream, thereby increasing the blockage in the passage. While the mass flow through the clearance gap decreases with a reduced

effective clearance, the blade tip leakage flow travels further to interact with the leading-edge vortex, increasing the loss from the vortex and thus secondary flow. Simulations with 10% clearance remained within the high-clearance flow field regime, with blade tip leakage as the primary contributor to impeller loss. The effects of stronger secondary flow were only seen in the expanded mixing area of the blade tip leakage flow.

Sensitivity of the impeller to surface roughness and tip clearance is consistent with literature in the conclusions that a 1% change in tip clearance would result in a 0.8% change in efficiency, and increasing surface roughness from smooth to 10 μm would result in a 7% loss in efficiency.

6.1 Performance Summary for Varied Surface Roughness

The characteristics for simulations with an R_a of 1 and 10 μm are plotted against the baseline hydraulically smooth surface simulation. Figure 6.1 shows that with increasing surface roughness, efficiency decreases but head rise increases for ϕ lower than 0.18. At higher ϕ, head rise decreases with increased roughness. Figure 2.5 shows experimental data consistent the simulation results an increase in surface roughness improved performance.

Pitch-wise averaged meridional plots for the flow field are provided in Figures 6.2 to 6.4 for 5% tip clearance for the operating points at a ϕ equal to 0.2. This operating point was selected for its high efficiency across each roughness simulation. The baseline 5% tip clearance, smooth surface simulation at the chosen operating point is seen in Figures 5.2 to 5.4. The definitions for flow rate and pressure rises are consistent with those used in Chapter 5.

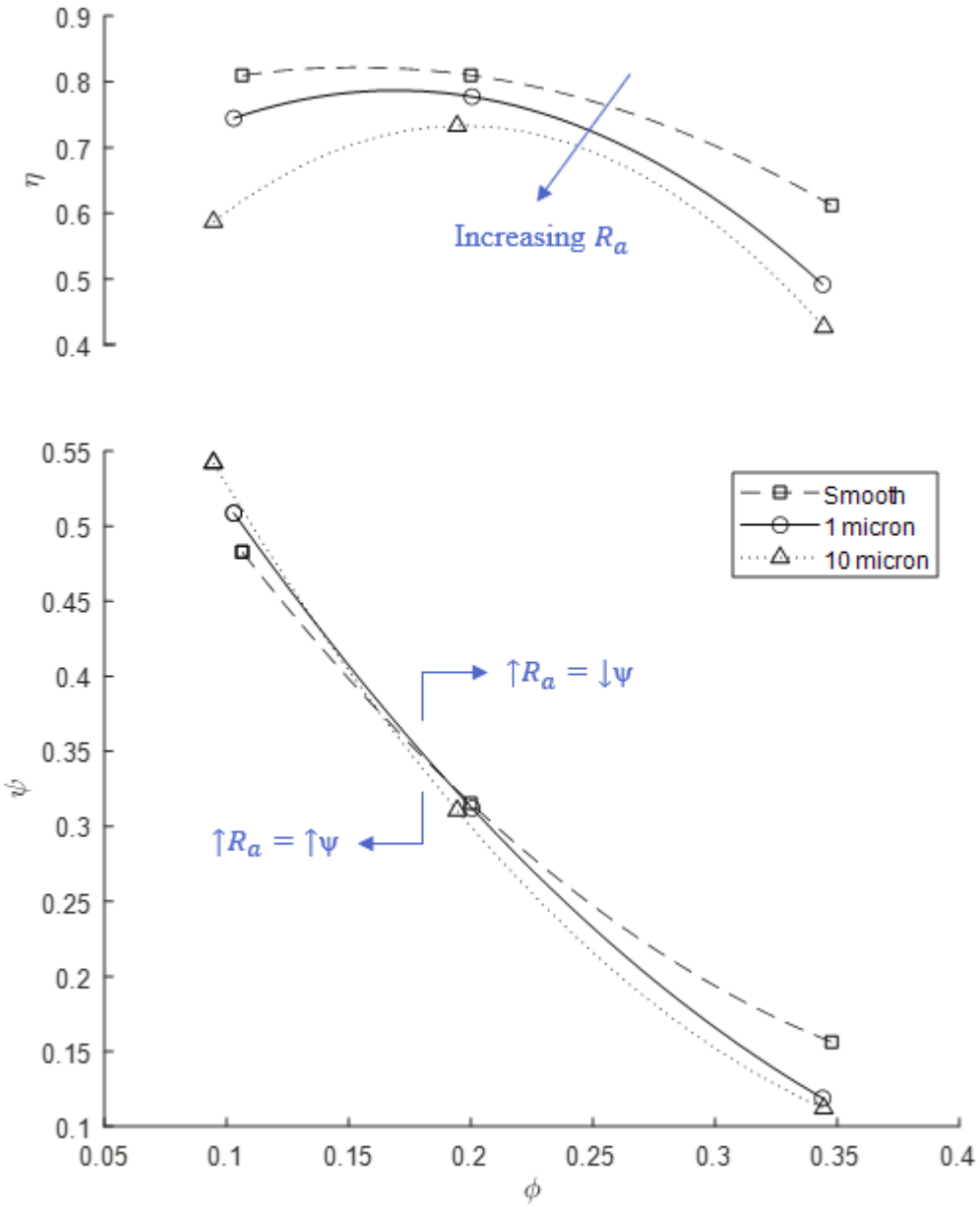

Figure 6.1: Characteristics show a similar head rise between simulations despite a drop in deficiency at rougher surface finishes.

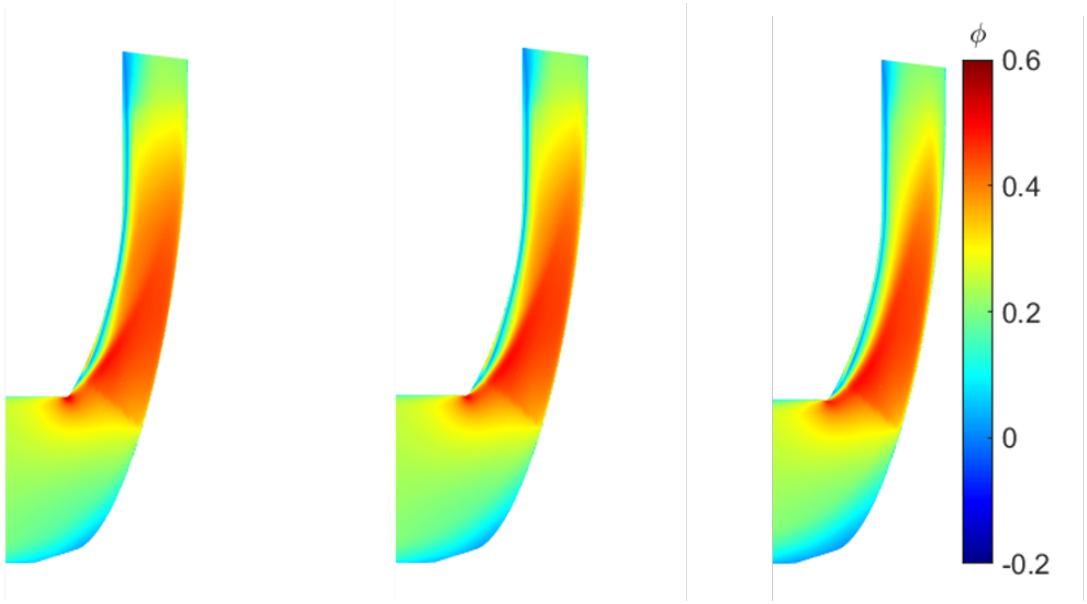

(a) Smooth surface (b) $R_a = 1\ \mu m$ (c) $R_a = 10\ \mu m$

Figure 6.2: Velocity is similar between surface roughness simulations at an operating point of $\phi = 0.2$.

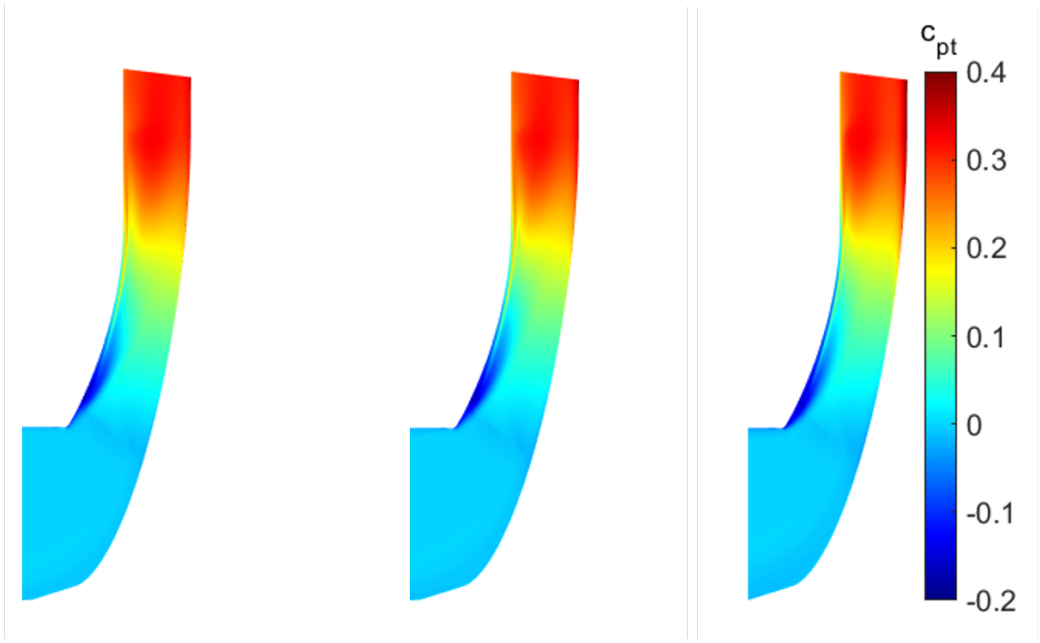

(a) Smooth surface (b) $R_a = 1\ \mu m$ (c) $R_a = 10\ \mu m$

Figure 6.3: Stagnation pressure is similar between surface roughness simulations at an operating point of $\phi = 0.2$.

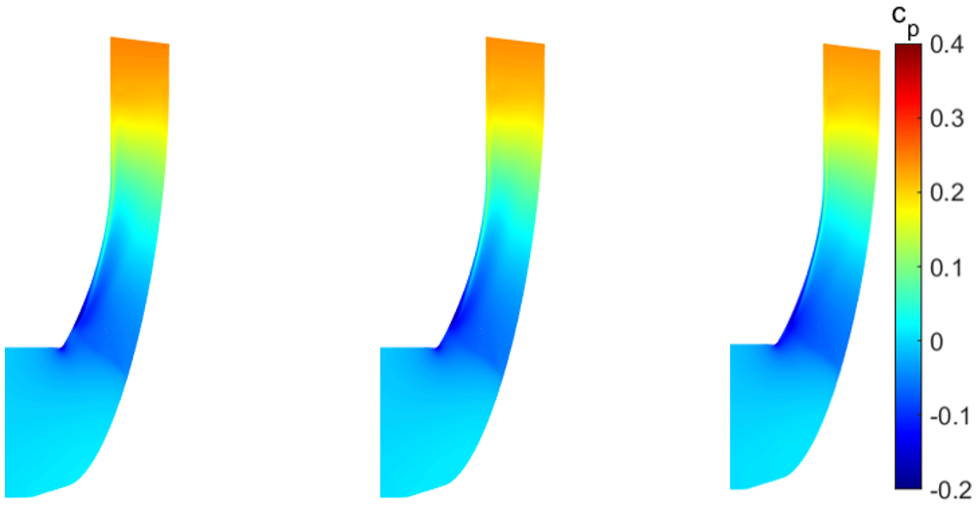

(a) Smooth surface (b) $R_a = 1\ \mu m$ (c) $R_a = 10\ \mu m$

Figure 6.4: Static pressure is similar between surface roughness simulations at an operating point of $\phi = 0.2$.

6.2 Reduced Effect of Blade Tip Leakage Flow

At the entrance to the tip clearance gap, the fluid flows over a sharp corner of the blade pressure surface, resulting in the formation of a separation bubble called a vena contracta which further contracts the flow within the tip gap. With increased surface roughness, more near-wall turbulence is introduced to the flow, which in turn decreases the height of the vena contracta. This is depicted in Figure 6.5 showing the relative flow velocity normal to the camber line ($w^* = w_n/U$) inside the clearance gap for the three clearances and three roughness cases at a ϕ of 0.2. The velocity of the blade tip leakage flow is reduced with increasing roughness due to the smaller vena contracta, lessening the impact of the tip clearance vortex mixing with the passage flow. Additionally, the vorticity from the increased turbulence causes the viscous layer to thicken. This can be seen clearly at the shroud wall in Figure 6.5, further reducing the effect of the blade tip leakage flow on overall loss.

The Storer-Cumpsty model is employed to estimate the contribution of blade tip leakage to overall losses. The results are presented in Table 6.1 for varying surface roughness and

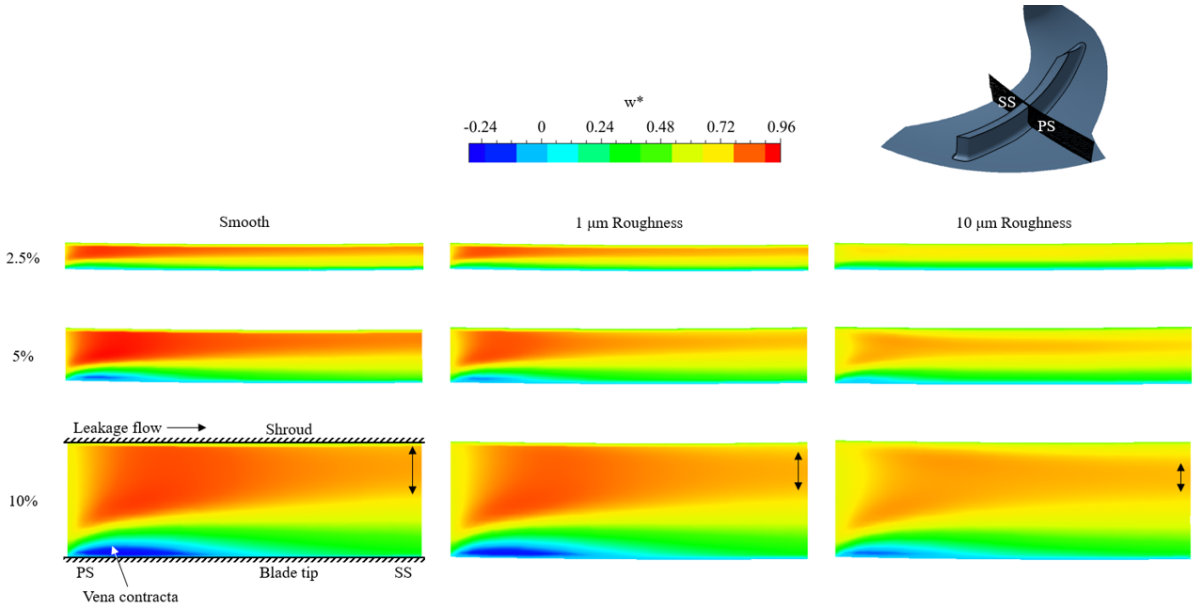

Figure 6.5: Reduced effect of the blade tip leakage flow on total impeller loss at increased roughness is due to a smaller vena contracta height at a $\phi = 0.2$.

Surface R_a	2.5% Tip clearance	5% Tip clearance	10% Tip clearance
smooth	50%	82%	88%
1 μm	31%	58%	77%
10 μm	15%	36%	56%

Table 6.1: The estimate percent contributions of blade tip leakage flow to overall impeller loss for different levels of surface roughness at a $\phi = 0.2$.

tip clearances. Although the control volume does not directly account for surface roughness, the model parameters were recalculated for each surface case to account for the effects of roughness. The mass flow for simulations with rough surfaces is reduced compared to the smooth surface simulation, confirming the effects of a reduced vena contracta height. The proportion of overall losses attributed to blade tip leakage flow decreases with increasing surface roughness, indicating that surface roughness becomes the dominant contributor to overall loss compared to blade tip leakage flow.

When the impact of blade tip leakage flow on impeller performance is reduced, the flow field in a rough surface simulation will resemble that of a smooth surface simulation with a

smaller tip clearance gap. This change in flow field regime is evident in the 5% tip clearance scenario. For all flow coefficients for an R_a of $10\mu m$, a leading-edge vortex forms and does not transition into blade tip leakage flow (Figure 6.6). The reduced blade tip leakage flow due to the 10 μm surface no longer carries the vorticity through the tip clearance gap. Previously, this flow field was only observed in simulations with a 2.5% tip clearance with a smooth surface, indicating that for a surface roughness R_a of 10 μm, the tip clearance that distinguishes low clearance and high clearance flow field regimes increases from 2.5% to 5% tip clearance.

At a ϕ of 0.35, the leading edge vortex appears at an R_a of 1 μm, as the increased passage flow rate dominates that of the blade tip leakage flow rate and the leading-edge vortex travels downstream. At higher mass flows, the distinguishing R_a between flow field regimes is 1 μm.

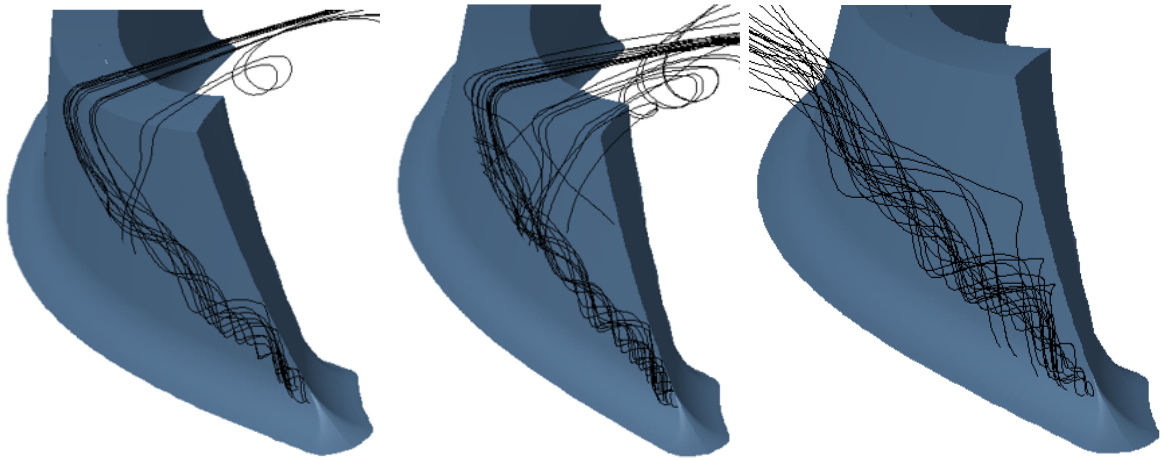

(a) Smooth surfaces (b) 1 μm surface roughness (c) 10 μm surface roughness

Figure 6.6: For 5% tip clearance at the best point of $\phi = 0.2$, the low clearance flow field regime is distinguished from the high clearance regime at an R_a of 10 μm. At a $\phi = 0.35$, an R_a of 1 μm distinguishes the regimes.

6.3 Increased Blockage due to a Strengthened Secondary Flow

With increased roughness, the hub boundary layer thickens, strengthening the secondary flow. Because of a stronger secondary flow, the blade tip leakage flows further across the passage before it mixes with the main stream, increasing blockage within the passage.

Figure 6.7 illustrates the 5% tip clearance case, presenting 50% span entropy contour plots and relative streamlines depicting entropy rise for a ϕ of 0.2. Non-dimensional entropy rise is defined in Equation 5.1. For an average roughness R_s of 10 μm, the relative streamlines of the blade tip leakage flow span the passage to interact with the leading-edge vortex, increasing the blockage resulting from the leading-edge vortex. An arrow in Figure 6.7 highlights the streamlines composing this interaction.

In the 2.5% clearance case for a ϕ of 0.2, surface roughness reduces effective clearance, notably diminishing the corner vortex caused by blade tip leakage, seen in Figure 6.8c. Strengthened secondary flow additionally causes the blade tip leakage to penetrate deeper into the mainstream, enhancing its interaction with the leading-edge vortex. Consequently, at this clearance, the leading-edge vortex becomes more pronounced, shifting the primary source of loss from blade tip leakage to secondary flow. This shift is evident in the entropy distribution, where the region of loss associated with the leading-edge vortex surpasses that of blade tip leakage, as shown in the 50% span contour plots of Figure 6.8.

In the simulation with an R_a of 10 μm, double blade tip leakage is present in the downstream section of the blade (Figure 6.8c). Although double blade tip leakage does not influence impeller loss, its appearance, despite reduced impact of blade tip leakage flow, shows the dominance of the secondary flow on the impeller flow field at increased surface roughness. Because of a strengthened secondary flow, the blade tip leakage flow reaches the subsequent blade, preventing blade tip leakage flow from mixing with the main stream at the downstream part of the blade.

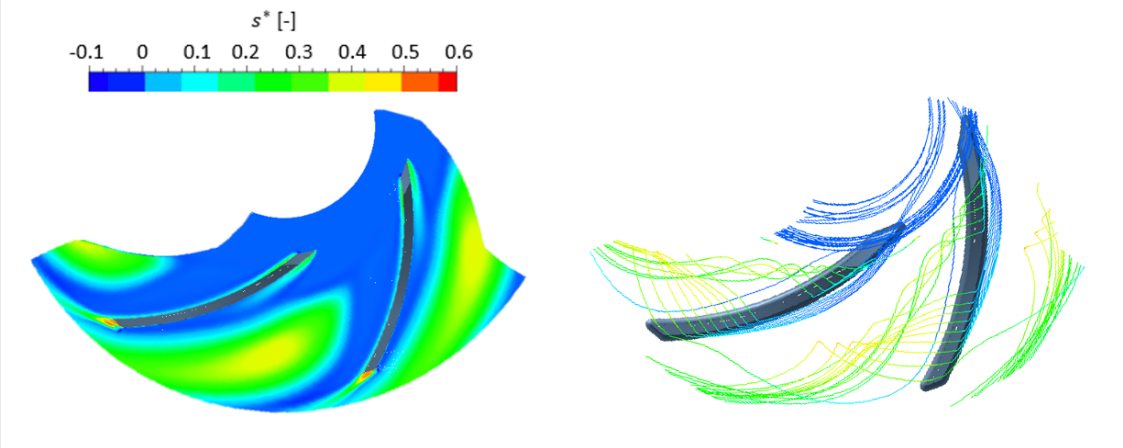

(a) Smooth surfaces

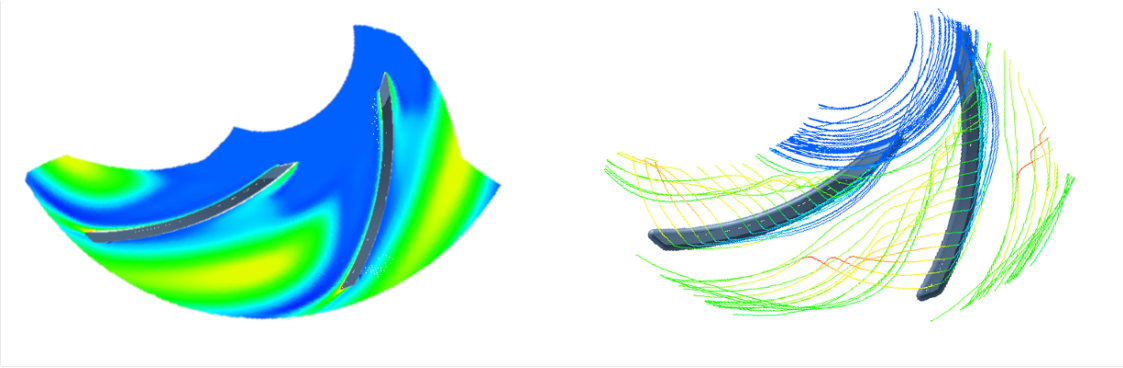

(b) 1 μm surface roughness

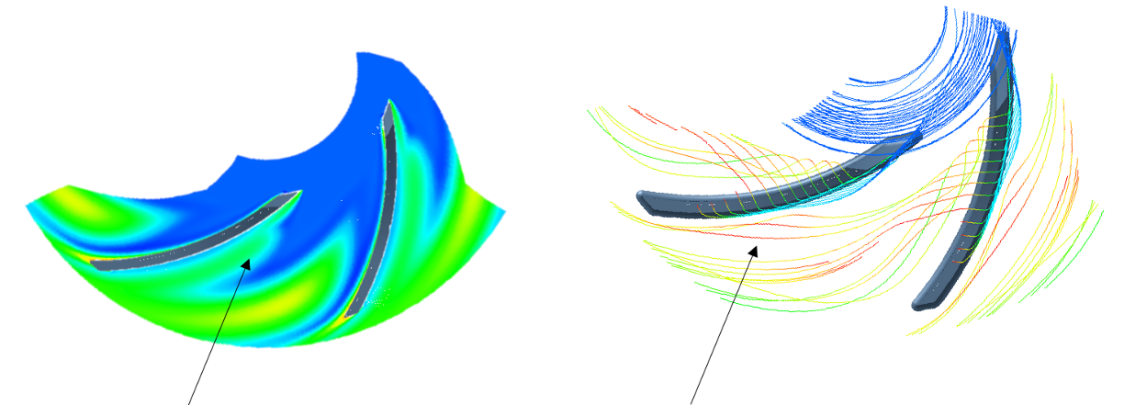

(c) 10 μm surface roughness

Figure 6.7: Blockage increases with surface roughness due to a stronger secondary flow. Plots are for 5% clearance at an operating point of $\phi = 0.2$.

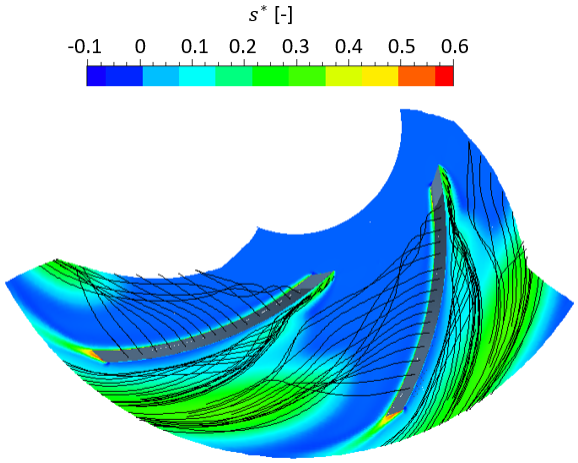

(a) Smooth surfaces

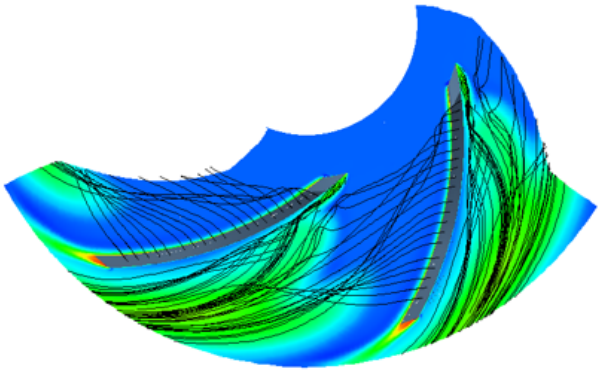

(b) 1 μm surface roughness

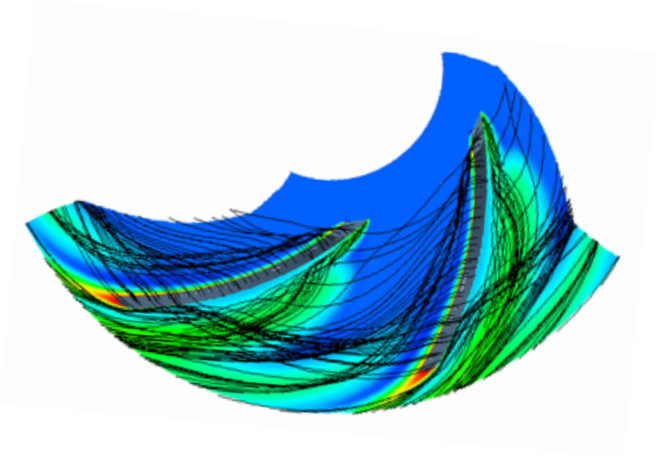

(c) 10 μm surface roughness

Figure 6.8: At 2.5% tip clearance and surfaces with an R_a of 10 μm, the blade tip leakage vortex is minimized, making secondary flow the primary source of loss at a $\phi = 0.2$.

6.4 Large Tip Clearance Flow Field Regime

For 10% clearance, the flow field remains in the regime characteristic for large clearances over all surface roughness simulations. The mixing of the blade tip leakage flow into the main stream remains the predominant source of loss despite the reduced effect of blade tip leakage flow on overall impeller loss due to roughened surfaces. In Figure 6.9, increasing surface roughness increases loss and blockage due to a stronger secondary flow.

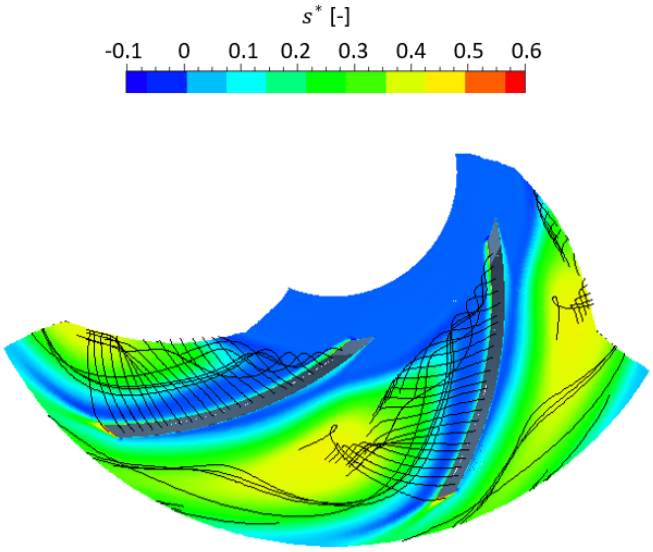

(a) Smooth surfaces

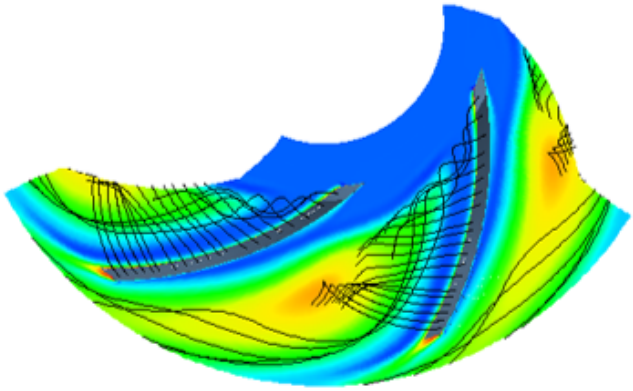

(b) 1 μm surface roughness

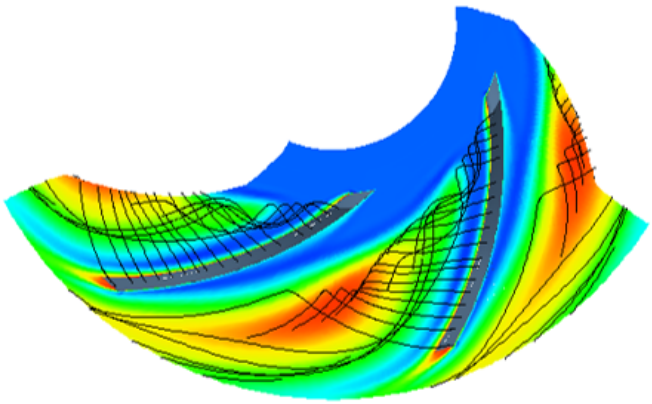

(c) 10 μm surface roughness

Figure 6.9: For all surface finishes with 10% tip clearance at $\phi = 0.2$, the dominant contributor to loss is blade tip leakage flow mixing (large clearance flow field regime).

6.5 Sensitivity of Loss to Surface Roughness and Tip Clearance

A summary of roughness effects at varying tip clearances is illustrated in Figure 6.10. At a given roughness, a 1% change in tip clearance results in a 0.8% loss in efficiency, which is in agreement with the impeller turbopump results of Hoshide and Nielson [9], Chen et al. [11], Williams et al. [13], [14], and Engeda et al. [15] (Table 2.1).

Across all tip clearances, there is an approximate 7% loss in efficiency when increasing surface roughness to 10 μm at a given clearance, consistent with efficiency loss provided by Gulich [21], He [22], Bammert and Milsch [23], and Bammert and Woelk [24] (Table 2.2).

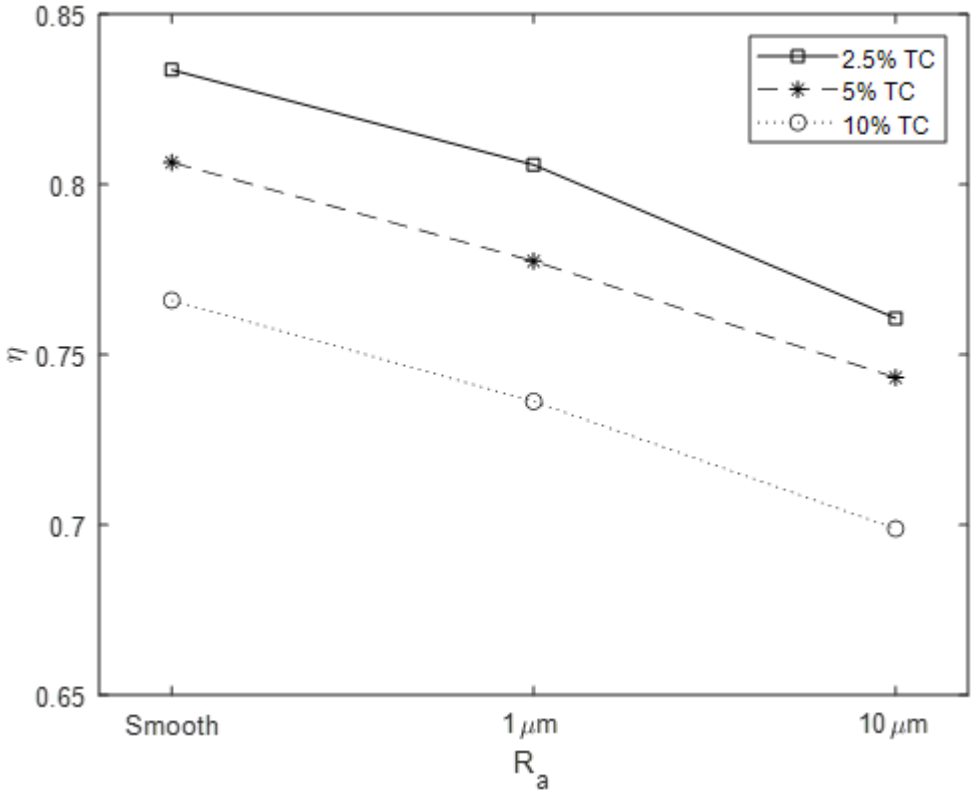

Figure 6.10: Efficiency drop due to roughness at different clearances at an operating point of $\phi = 0.2$.

Chapter 7

Conclusions

7.1 Summary

The thesis demonstrates that the primary contributors to loss in a centimeter-scale impeller are blade tip leakage flow and secondary flow. Efficiency decreases with increasing blade tip clearance and surface roughness. Blade tip clearance can vary during operation, while surface roughness is set by the manufacturing process. Small-scale impellers are sensitive to changes in blade tip clearance and roughness due to the relative magnitude of changes compared to the overall size of the impeller.

The key learnings are:

- The sensitivity of small-scale impellers to a 1% change in tip clearance results in a 0.8% loss in efficiency. Increasing surface roughness from an R_a value of 1 to 10 μm results in a 4% loss in efficiency.

- Mixing from blade tip leakage flow prevails as the dominant loss mechanism at 10% clearance. Secondary flow is the dominant loss mechanism for clearance less than 5%. With increasing surface roughness, the blade tip clearance that distinguishes which loss mechanism dominates decreases. The presence of the leading-edge vortex is indicative of secondary flow dominating overall loss.

- Surface roughness has a greater impact on loss than blade tip leakage flow. At a surface roughness R_a of 10 μm, the contribution of blade tip leakage flow to total impeller loss is 15% for 2.5% tip clearance, 36% for 5% tip clearance, and 56% for 10% tip clearance, the majority of loss due to secondary flow.

7.2 Implications of Present Work

The current state-of-the-art manufacturing methods for impellers with tip speeds below 300 $\frac{m}{s}$ include machining or casting of aluminum or corrosion-resistant alloys, such as Monel. For higher tip speeds, high-strength forged materials are machined [34]. Lathes and mills can achieve average surface roughness values ranging from 0.5 to 8 μm [18]. Subtractive manufacturing methods also offer a broader selection of materials suitable for rocket engine environments given the extreme operating conditions seen by the turbopump impellers. Among AM processes, only binder jetting can achieve surface finishes comparable to machining, reaching surface roughness levels as low as 1 μm [18], however binder jetted parts have poorer mechanical properties compared to other AM processes. Furthermore, many materials compatible with additive manufacturing (AM) are unsuitable for applications requiring high-strength and corrosion-resistant properties. If choice in manufacturing method is limited, prioritizing a smaller blade tip clearance becomes important.

7.3 Recommendations for Future Work

The following list summarizes suggestions for future work:

- Conduct experiments to validate computational models and to determine the relationship between R_a and k_s for the small-scale impeller under investigation.
- The Spalart-Allmaras model was selected for its robustness, but further investigation into other turbulence models is recommended to assess whether modeling error of the

blade tip clearance flow and surface roughness models changes.

- The NUMECA software imposes a minimum wall cell size requirement of at least $\frac{k_s}{15}$. This limitation resulted in low resolution of the boundary layer and hindered the quantification of changes in effective clearance due to surface roughness. Detailed resolution of the boundary layer flow is necessary to gain insights into the critical effective clearance where low-clearance flow features emerge.

- Blade features like solidity and exit angle could be optimized to mitigate loss from blade tip leakage flow. Additionally, a trade-off study on the use of shrouded pumps for small-scale rocket applications could provide valuable insights.

Appendix A

Jet-Wake Mixing-out Model

To characterize the loss from mixing out non-uniform flow based on varying velocity profiles, an inviscid jet profile was applied.

A control volume can be effectively employed to validate the results of averaging methods used for mixing out non-uniformity of exit flow from CFD. Figure A.1 illustrates the setup. The model simplifies the more complex flow field into two distinct flow components: a primary jet, denoted as $u_{i,p}$, and a secondary slower flow, denoted as $u_{i,s}$. By decomposing the inlet flow into these two components, the analysis reduces the complexity of the flow field, allowing for a more tractable examination of the system's behavior.

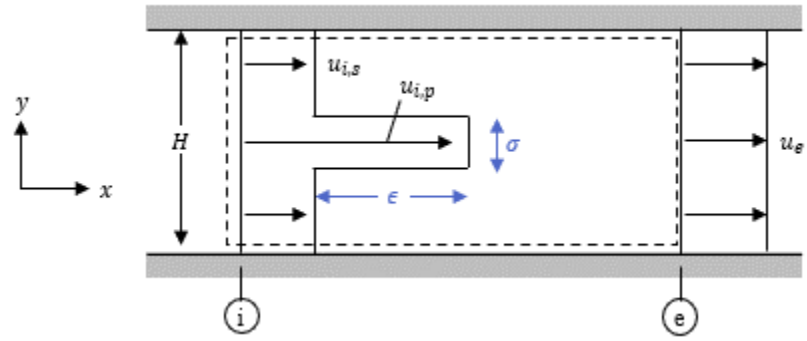

Figure A.1: Jet control volume schematic.

Figure A.2 provides three-dimensional contour plots that show the translation of the complex exit flow of the pump into the two inlet flows of the jet control volume. Note that

the images in Figure A.2 are in grid format following the exit plane mesh, and so the edges of the figures are *not* the blades but rather the bounds of the periodic boundary condition. The lower flow near the shroud is the result of leakage mixing described in Chapter 5.

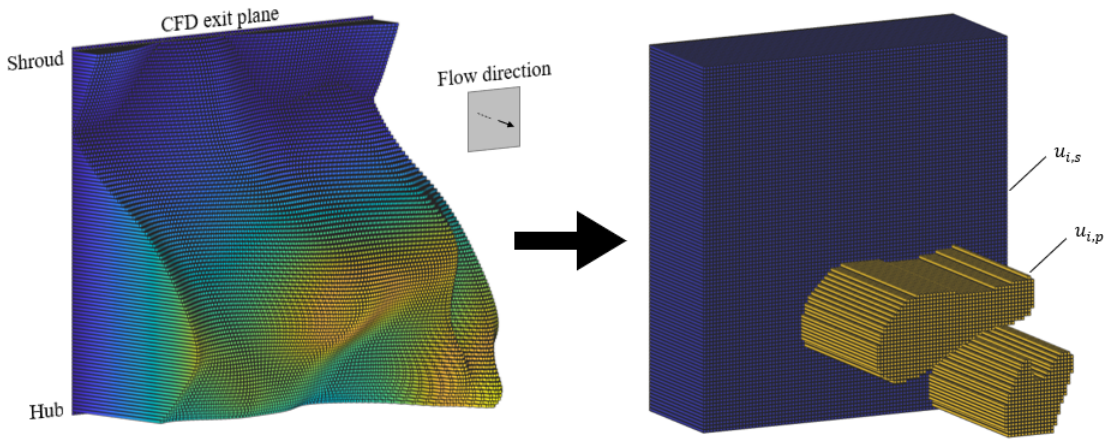

Figure A.2: Complex, non-uniform velocity field at CFD exit simplified to two velocities for jet validation of mixing out losses.

The relationship between these two flows in the jet control volume is defined by two parameters: the area ratio, σ, and the velocity ratio, ϵ, defined below in Equation A.1.

$$\sigma = \frac{A_{i,p}}{A_s} \qquad \epsilon = \frac{u_{i,p}}{u_s} \tag{A.1}$$

Using this model, a control volume sweep is conducted across varying values of the area ratio (σ) and the velocity ratio (ϵ) resulting in the loss profile depicted in Figure A.3. Inputs to this sweep were the static pressure boundary condition imposed on the solver, the exit plane area of the pump, and the separation velocity defining the cutoff between the primary and secondary flows. Validation checks at $\sigma = 0, 1$ showed no loss, as expected. The data indicate that higher losses occur at elevated velocity ratios, primarily due to the increased shear friction between the jet flow and the slower surrounding fluid. Significant impact on loss is observed when the area ratio ranges between 10% and 30%, where the jet velocity exerts maximum influence. Beyond this range, the jet velocity effectively dominates as the 'main flow,' leading to a reduction in losses due to diminished relative shear effects.

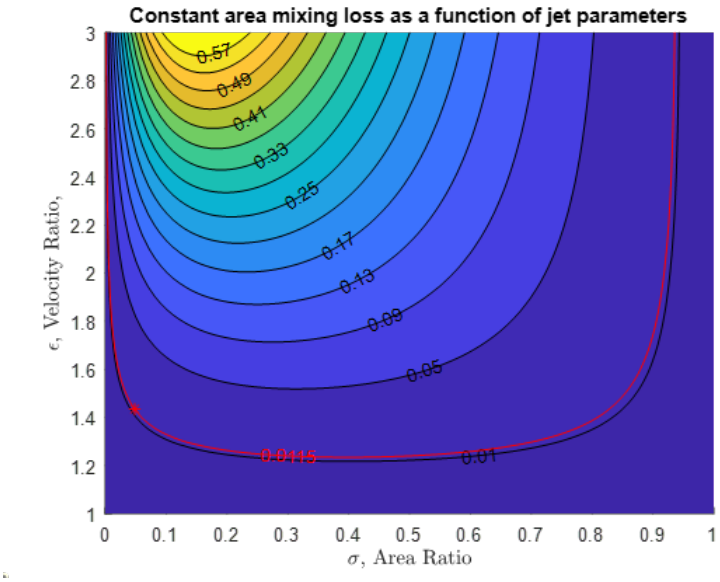

Figure A.3: Jet control volume σ and ϵ sweep.

Mass averaging velocities across the computational exit plane yielded an jet area constituting 10.6% of the passageway, with a velocity 1.42 times faster than the surrounding flow. These values of σ and ϵ are shown by a red star on Figure A.3. The resultant loss from the jet model is 1.15%, the corresponding contour line is highlighted in red. The mixed-out averaged loss outlined in Chapter 4 similarly results in a loss of 1.21%.

References

[1] Johann Friedrich Gülich, *Centrifugal Pumps*, Third. Springer.

[2] NASA, *Turbopump Systems for Liquid Rocket Engines*, Aug. 1974. URL: https://ntrs.nasa.gov/api/citations/19750012398/downloads/19750012398.pdf.

[3] Rocketdyne Propulsion & Power, *Space Shuttle Main Engine Orientation*, Jun. 1998. URL: http://large.stanford.edu/courses/2011/ph240/nguyen1/docs/SSME_PRESENTATION.pdf.

[4] R. Liu, Z. Wang, T. Sparks, F. Liou, and J. Newkirk, "Aerospace applications of laser additive manufacturing," *Laser Additive Manufacturing*, pp. 351–371, 2017.

[5] Shahir Mohd Yusuf, Samuel Cutler, and Nong Gao, "Review: The Impact of Metal Additive Manufacturing on the Aerospace Industry," *Metals*, Nov. 2019. DOI: https://doi.org/10.3390/met9121286.

[6] J.D. Denton, "Loss Mechanisms in Turbomachines," in *Volume 2: Combustion and Fuels; Oil and Gas Applications; Cycle Innovations; Heat Transfer; Electric Power; Industrial and Cogeneration; Ceramics; Structures and Dynamics; Controls, Diagnostics and Instrumentation; IGTI Scholar Award*, May 1993, p. 40. DOI: https://doi.org/10.1115/93-GT-435.

[7] J. A. Storer and N. A. Cumpsty, "An Approximate Analysis And Prediction Method For Tip Clearance Loss In Axial Compressors," Cincinnati Ohio: ASME, May 1993.

[8] M V Casey and C J Robsinson, "A unified correction method for Reynolds number, size, and roughness effects on the performance of compressors," *Proceedings of the Institution of Mechanical Engineers*, vol. 225, no. Part A: Journal of Power and Energy, Apr. 2011.

[9] R. K. Hoshide and C. E. Nielson, "Study Of Blade Clearance Effects On Centrifugal Pumps," NASA Lewis Research Center, Final Report NASA CR-120815 R-8806, Mar. 1973.

[10] Björn-Christian Will, Friedrich-Karl Benra, and Hans-Josef Dohmen, "Investigation of the Flow in the Impeller Side Clearances of a Centrifugal Pump with Volute Casing," *Journal of Thermal Science*, vol. 21, no. 3, pp. 197–208, 2012. DOI: 10.1007/s11630-012-0536-3.

[11] Wei-Chung Chen, M.Williams, John K. Paris, G.H.Prueger, and R.Williams, "Development and Validation of High Performance Unshrouded Cetrifugal Impeller," Salt Lake City, Utah: AIAA, Jul. 2001. DOI: 10.2514/6.2001-3399.

[12] Joost J. Brasz, "Investigation into the Effect of Tip Clearance on Centrifugal Compressor Performance," Amsterdam, The Netherlands: The American Society for Mechanical Engineers, Jun. 1988.

[13] Robert W. Williams, Stephen E. Skelley, Eric T. Stewart, Alan R. Droege, George H. Prueger, Wei-Chung Chen, Morgan, and Morgan Williams, "High Head Unshrouded Impeller Pump Stage Technology," Huntsville, AL: AIAA, Jul. 2000.

[14] Robert W. Williams, Stephen E. Skelley, Wei-Chung Chen, and Morgan Williams, "Comparison of Unshrouded Impeller Analysis and Experiment," Salt Lake City UT: American Institute of Aeronautics and Astronautics, Jul. 2001.

[15] A. Engeda, W. P. Strate, and M. Rautenberg, "Correlation of Tip Clearance Effects to Impeller Geometry and Fluid Dynamics," *The American Society for Mechanical Engineers*, Jun. 1988.

[16] Y. Senoo and M. Ishida, "Deterioration of Compressor Performance Due to Tip Clearance of Centrifugal Impellers," *Journal of Turbomachinery*, vol. 109, Jan. 1987.

[17] M. Ishida, H. Ueki, and Y. Senoo, "Effect of Blade Tip Configuration on Tip Clearance Loss of a Centrifugal Impeller," *Transactions of the ASME*, vol. 112, pp. 14–18, Jan. 1990.

[18] Paul R. Gradl, Omar R. Mireles, Christopher S. Protz, and Chance P. Garcia, *Metal Additive Manufacturing for Propulsion Applications* (Progress in Astronautics and Aeronautics). AIAA, Jul. 2022, vol. 263, ISBN: 978-1-62410-626-2.

[19] JP Bons, "A Review of Surface Roughness Effects in Gas Turbines," *Journal of Turbomachinery*, vol. 132, Apr. 2010. DOI: 10.1115/1.3066315.

[20] Thomas Adams, Christopher Grant, and Heather Watson, "A Simple Algorithm to Relate Measured Surface Roughness to Equivalent Sand-grain Roughness," *International Journal of Mechanical Engineering and Mechatronics*, vol. 1, no. 1, 2012. DOI: 10.11159/ijmem.2012.008.

[21] Johann Friedrich Gülich, "Effect of Reynolds Number and Surface Roughness on the Efficiency of Centrifugal Pumps," *Journal of Fluids Engineering*, vol. 125, Jul. 2003. DOI: 10.1115/1.1593711.

[22] Xiaoke He, Weixuan Jiao, Chuan Wang, and Weidong Cao, "Influence of Surface Roughness on the Pump Performance Based on Computational Fluid Dynamics," *IEEE Access*, vol. 7, pp. 105 331–105 341, 2019. DOI: 10.1109/ACCESS.2019.2932021.

[23] K. Bammert and R. Milsch, "Boundary Layers on Rough Compressor Blades," in *The American Society of Mechanical Engineers*, 1972.

[24] K. Bammert and G. U. Woelk, "The Influence of the Blading Surface Roughness on the Aerodynamic Behavior and Characteristic of an Axial Compressor," *Journal of Engineering for Power*, vol. 102, no. 2, pp. 283–287, Apr. 1980.

[25] Hermann Schlichting and Klaus Gersten, *Boundary Layer Theory*, 9th ed. Springer, 2017.

[26] Markus Diehl, Christoph Schreiber, and Jurg Schiffmann, "The Role of Reynolds Number Effect and Tip Leakage in Compressor Geometry Scaling at Low Turbulent Reynolds Numbers," *Journal of Turbomachinery*, vol. 142, p. 11, Mar. 2020.

[27] Lewis F. Moody, "Friction Factors for Pipe Flow," *Journal of Fluids Engineering*, vol. 66, no. 8, pp. 671–678, Nov. 1944. DOI: https://doi.org/10.1115/1.4018140.

[28] Yunus A. Çengel and John M. Cimbala, *Fluid Mechanics Fundamentals and Applications*, 4th ed. McGraw Hill, 2018.

[29] Cadence, *User Guide Autogrid5 v18.1*.

[30] Marek Paty, Bogdan C. Cernat, Cis De Maesschalck, and Sergio Lavagnoli, "Experimental and Numerical Investigation of Optimized Blade Tip Shapes—Part II: Tip Flow Analysis and Loss Mechanisms," *Journal of Turbomachinery*, vol. 141, Jan. 2019. DOI: 10.1115/1.4041466.

[31] NUMECA International, *User Manual FINE™/Turbo v9.1*, Nov. 2014.

[32] Edward Greitzer, Choon S. Tan, and Martin B. Graf, *Internal Flow: Concepts and Applications*. Cambridge University Press, 2004.

[33] N. A. Cumpsty and J. H. Horlock, "Averaging Nonuniform Flow for a Purpose," *Journal of Turbomachinery*, vol. 128, pp. 120–129, Jan. 2006. DOI: 10.1115/1.2098807.

[34] W. E. Campbell and J. Farquhar, *Centrifugal Pumps for Rocket Engines*, 1974. URL: https://ntrs.nasa.gov/api/citations/19750003130/downloads/19750003130.pdf.